Delft University of Technology

Design of Josephson Parametric Amplifier for High Fidelity Fluxonium Readout

Master's Thesis

M. Doruk Uğur (SN 5812798)

Supervisor: Christian Kraglund Andersen

Daily Supervisor: Taryn V. Stefanski

Daily Supervisor: Lukas J. Splitthoff

November 2023 - June 2024

Contents

Abstract

Since the early 2000s, High Electron Mobility Transistors (HEMTs) have been the preferred choice for the first-stage amplification of qubit readout resonators at cryogenic temperatures. However, Josephson Parametric Amplifiers (JPAs) have recently emerged as a more attractive alternative due to their quantum-level noise performance. Despite their advantages, JPAs face significant challenges such as narrow bandwidths, low dynamic ranges, and limited gains, which hinder their widespread adoption. By presenting an optimized JPA chip design with a Kerr coefficient of 1000 Hz and a Kappa value of 100 MHz that operates in the 4-8 GHz range, this thesis seeks to address these issues. The design methodology involves an iterative process using Comsol and Microwave Office softwares to refine the design and the resulting Kappa and Kerr coefficients at each phase of development. This approach results in a JPA design that overcomes the traditional limitations, making it a viable candidate for broader applications in quantum technology.

Motivation

In quantum superconducting circuits, various types of qubits have been developed for quantum error correction. To achieve optimal performance, it is essential to design structures that support high-fidelity gate operations, accurate readout, and extended qubit coherence times. In recent years, the fluxonium qubit has become one of the top choice, even though it's more complex than the well-known transmon and flux qubits developed earlier. Operating at the sweet spot affords low frequency and a small charge matrix element, making fluxoniums insensitive to charge noise and thus, leading to long coherence times. The long time allows for long storage of information which enables high gate and readout fidelities. In addition, larger anharmonicity compared to transmon qubits defines the computational subspace well and principally allows for fast gates [1]. However, one notable challenge is obtaining weak readout signals, which requires amplification before a lossy and noisy environment affects the signal. Standard readout chains involving only a 4K stage high-electron-mobility transistor (HEMT) amplifier and other HEMT amplifiers at room temperature are incapable of providing the required amplification and also introduce noise levels that significantly exceed the quantum limit. Hence, we need a parametric amplifier which offers quantum-limited noise and importantly dissipates minimal energy. It can be used effectively at the initial stages of the amplification chain for boosting the signal-to-noise ratio by its gain suppressing the noise of the higher temperature stage in the chain [2]. However, despite their seemingly ideal attributes, they need to be optimized to get accurate results and higher fidelity in the state-of-the-art qubits' readout process. In this project, we aim to improve a parametric amplifier for fluxonium qubits readout signal whose bandwidth is around 10MHz and photon number is between 100 and 200. Therefore, we will develop a superconducting parametric amplifier with a bandwidth of 100 MHz and a Kerr coefficient of 1000 Hz.

Introduction

This thesis presents a comprehensive study on the design, optimization, and application of Josephson Parametric Amplifiers (JPAs) with a focus on enhancing the readout of fluxonium qubits, a crucial aspect in the field of quantum computing. The objective of this research is to address the specific challenges associated with the quantum measurement process by developing an advanced JPA design that operates effectively within the specified frequency range and environmental conditions.

Chapter 1 begins with a theoretical exploration of fluxonium qubits, detailing their unique properties and the intricacies of their readout mechanisms. This is followed by an in-depth discussion on the principles of parametric amplification. The chapter progresses to elaborate on the bandwidth, gain, dynamic range, and noise properties of Josephson Parametric Amplifiers, establishing the foundational concepts that underpin the subsequent design and optimization efforts. Further, this chapter delineates the critical components of the JPA and the experimental setup into which the JPA is integrated, providing a holistic view of the operational environment and the interactions within it.

Chapter 2 shifts focus towards the practical aspects of this research, starting with the definition of the target parameters that guide the JPA design. A concise overview of the computer-aided design tools used is provided, emphasizing their role in streamlining the design process. The methodology adopted for the JPA design is thoroughly discussed, with particular attention paid to the influence of various parameters on the target values. This chapter culminates in a detailed presentation of the final designs, alongside reflective commentary on the collective features of the four developed JPAs.

Chapter 3 is dedicated to the enclosure design for the JPA chips, which are required to operate at cryogenic temperatures. Initial sections reiterate the target parameters and the computational strategies used in design planning. Simulation outcomes are reviewed, leading up to the unveiling of the final enclosure design. Additionally, this chapter discusses alternative approaches that were considered, providing insights into the decision-making process and the rationale behind the chosen design solutions.

The conclusion synthesizes the findings from both the amplifier and enclosure designs. It highlights the key points of the designs and discusses the solutions to some of the encountered challenges. The thesis concludes by reflecting on the broader implications of this work and suggesting avenues for future research, particularly in improving the performance and applicability of Josephson Parametric Amplifiers in quantum technology.

1 Theory of Parametric Amplifiers and Superconducting Qubits

1.1 Fluxonium qubit

A fluxonium qubit is one variant of superconducting qubits. Figure 1 adapted from the Ref.[1] shows the fluxonium qubit that is coupled to a readout resonator capacitively in order to enable dispersive readout for the qubit states. The primary distinction to the well-known transmon lies in the addition of a parallel inductor to the Josephson junction and capacitor, which alters its behavior. In cases where the frequency of system oscillation is lower than the plasma frequency, the parallel inductor functions similarly to an inductive wire. Such a large inductor is comparable to a low-pass filter in terms of circuitry. Consequently, the inductor short-circuits the low-frequency change in charge across the small junction, lowering the sensitivity of qubits to charge noise [3]. This makes its coherence time longer, which is an advantage for the readout and for doing more operations. Due to the charge insensitivity, a large shunting capacitance is not required to get a high E_j/E_c ratio, which reduces the charge dispersion. This leads to an increase in the anharmonicity of the circuit [4].

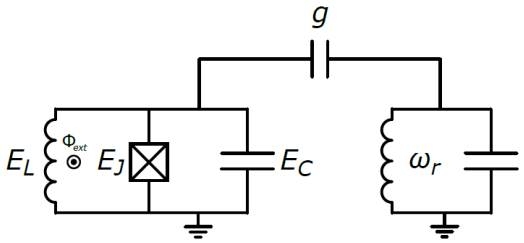

Figure 1: Circuit diagram of the fluxonium qubit [1]

The Hamiltonian of fluxonium qubits can be expressed as in Equation 1, which includes the charging energy E_c, the inductive energy E_l, and the Josephson energy E_j. ϕ_{ext} represents the external flux thread through the RF-SQUID loop created by Josephson junction and inductor [1, 5].

$$\hat{H}_{fluxonium} = 4E_c\hat{n}^2 + \frac{E_l\hat{\phi}^2}{2} - E_j cos(\hat{\phi} - \phi_{ext}) \tag{1}$$

The above Hamiltonian is written in terms of the charge operator $\hat{n} = \frac{-i(\hat{c}-\hat{c}^\dagger)}{\sqrt{2}\phi_0}$ and the flux operator $\hat{\phi} = \frac{\phi_0(\hat{c}+\hat{c}^\dagger)}{\sqrt{2}}$, where ϕ_0 is the magnetic flux quantum equals to $\frac{h}{(2e)}$, in harmonic oscillator basis. It can also be presented with $\hat{c}$ ($\hat{c}^\dagger$), which are ladder operators for fluxonium qubit subspace. The properties of the fluxonium qubit can be tuned in situ during the experiment using the external magnetic flux in the cosine part of the potential energy. By adjusting this term, the shape of the potential changes and, thus, the anharmonicity. When the fluxonium qubit is operated at $\phi_{ext} = \pi$, the potential shows a double-well structure as shown in Fig. 2 adapted from the Ref. [4], which gives larger anharmonicity, and that makes it less prone to leakage compared to transmons.

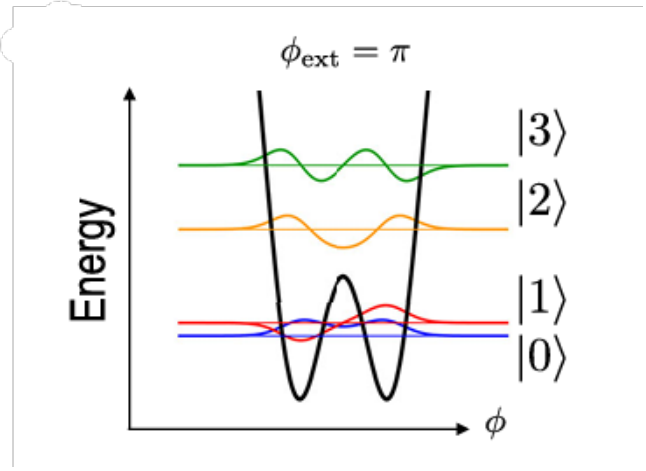

Figure 2: The fluxonium qubit's potential energy spectrum and eigenstates at $\phi_{ext} = \pi$ [4]

The special point is called the "sweet spot" or "flux degeneracy point" because the qubit frequency becomes insensitive to the first order of flux noise and this increases the coherence time of the qubit [6]. Instead, if the fluxonium qubit is biased at $\phi_{ext} = 0$, the potential -therefore at its properties- resembles those of a transmon qubit.

The Hamiltonian for the resonator is defined as:

$$\hat{H}_{resonator} = \hbar\omega_r(\hat{a}^\dagger\hat{a} + 1/2), \tag{2}$$

and the Hamiltonian describes the transverse coupling as:

$$\hat{H}_{coupling} = \hbar g(\hat{a}\hat{c}^\dagger - \hat{c}\hat{a}^\dagger), \tag{3}$$

Both the $\hat{H}_{resonator}$ and the $\hat{H}_{coupling}$ are used to describe the electrical circuit presented in Figure 1. The coupling Hamiltonian, which shows the interaction between the resonator and qubit, depends on g, coupling strength, and w_r, the resonator's resonant frequency.

For the readout of the qubit states, dispersive coupling has been used, which assumes the following parameter ordering $g \ll \omega_r, \omega_q$ and $|\Delta| = |\omega_r - \omega_q| \geq 1\,\text{GHz}$. In this regime following the Jaynes-Cummings model, the resonator frequency shifts depending on which state the qubit is in. This shift is called the dispersive shift. Unlike other types of qubits, the contribution of higher energy levels can significantly impact the dispersive shift [7]. If it is not operated around the sweet spot, the higher-lying transitions to non-computational states are added to the effective dispersive shift described in Figure 3 adapted from the Ref.[1]. The interaction of these transitions with the resonator leads to large dispersive shifts, which can be used to boost the readout fidelity [1].

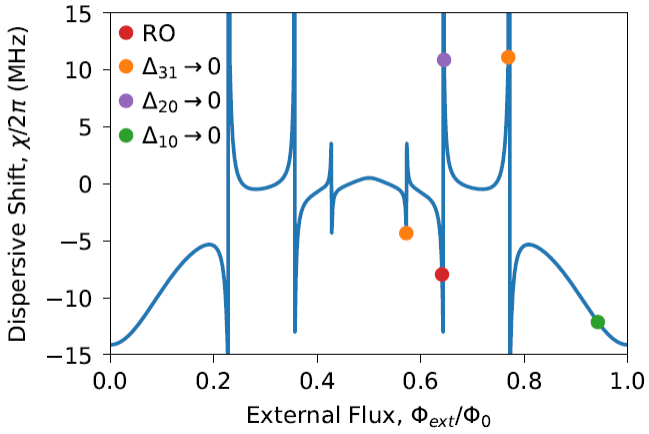

Figure 3: Dispersive shift vs. external flux for a certain realization of fluxonium qubit parameters [1]

In Figure 3, it can be seen that at the sweet spot (the shift is around 0.53 MHz) and for different external flux, different high-order transitions can contribute to the dispersive shift, with some transitions having greater contributions. For example, around the $\phi_{ext}/\Phi_0 = 0.78$ value, the $1 \to 3$ transition approaches resonance with the readout resonator and boosts the dispersive shift, and the same effect is true for the $0 \to 2$ transition around $\phi_{ext}/\Phi_0 = 0.65$. It is important to choose the proper dispersive shift to separate two states distinctively so that accurate results in the readout can be achieved. Therefore, the red point is the desirable spot due to the fact that both dispersive shifts are large, and this point is close to the sweet spot, which makes it easily adjusted by flux. In Figure 4 adapted from the Ref.[1], a drastic difference in SNR values at different readout points is seen. The SNR value at the sweet spot is almost zero due to the small dispersive shift, even if losses are neglected and thus the measurement efficiency is assumed to be 1. At the red point in Figure 3, in the ideal case, a high SNR value is obtained, but in practice, the signal will encounter many losses, the measurement efficiency is approximated to be 0.25, so the SNR value becomes lower (dashed blue line). As the overlap between the two quantum state distributions grows with the increase in the noise, there is a corresponding loss of certainty regarding the qubit's state. Separating these distributions can only be obtained by increasing signal amplitude. Therefore, the challenge is to increase this SNR value as much as possible and this can only be done with amplifiers [8].

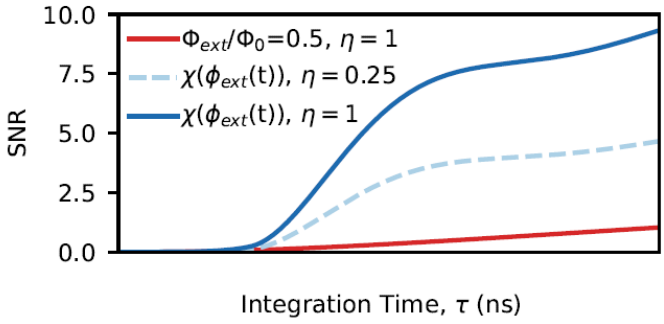

Figure 4: Signal-to-noise (SNR) ratio vs. integration time [1]

1.2 Parametric amplifier

Signals that are used to probe and the qubit state readout are generally small: a few photon energies per period. However, to detect the qubit state at room temperature, spatially far away from the qubit itself, amplifying the weak signal at cryogenic temperature is strictly required - while adding minimal noise. To achieve minimal added noise, ideally at the standard quantum limit, which is a consequence of the Heisenberg uncertainty relation, superconducting parametric amplifiers must be at the first amplification stage directly following the readout resonator. This allows the noise contribution through the amplification chain to be kept at a low level; hence, the signal-to-noise ratio is maximized.

In general, parametric amplifiers use parametric nonlinearity, which arises from the medium in optical systems or the elements in microwave circuits. This nonlinearity can give rise to various phenomena, among which the most significant is optical parametric oscillation observed in optical systems. In this effect, strong waves at the frequency ω_2 and intensity $I(\omega_2)$ alter the refractive index experienced by a weak probe wave at frequency ω_1. In Equation 4, the change in refractive index is proportional to second-order susceptibility $\chi^{(2)}$ generated by the nonlinearity of the optical system and current density of the strong pump field. This process is known as cross-phase modulation [9]. This modulation divides a pump photon ω_p into two new photons with different energies. The higher energy photon is referred to as the signal ω_s, and the lower energy photon is referred to as the idler ω_i.

$$\Delta n = C\chi^{(2)} I(\omega_2) \tag{4}$$

The same parametric process can be seen in microwave circuits using varactor diodes, which are p-n junction diodes used to provide the variable capacitive reactance. The capacitance of these varactor diodes varies nonlinearly according to the reverse bias voltage that is applied [10], which greatly amplifies the signal.

These amplification and mixing processes are called parametric processes because one periodically has to change a system parameter to achieve energy transfer. In other words, systems that have the ability to convert energy between conjugate field variables (including such voltage and current) can show parametric behavior provided that the mediating elements are modulable [11]. In an optical system, this is a refractive index, and in the circuit with varactor diodes, this can be capacitance. All these parameters vary with external fields, such as pump signals or reverse bias voltages, respectively.

Similarly, superconducting parametric amplification relies on the modulation of a parameter, specifically the inductance. The primary source of nonlinearity in many superconducting circuits is the Josephson junction, whose inductance depends on the current flowing through it. There are two types of parametric amplifier types.

The first type is the Josephson traveling wave parametric amplifier. It utilizes an extended array of Josephson junctions embedded in a coplanar waveguide to create a metamaterial transmission line [12, 13]. In principle, it can handle large input signals without saturation and provides amplification over a wide frequency range; careful design must ensure phase matching between the pump and signal waves.

The second type is the Josephson parametric amplifier (JPA). JPAs comprise superconducting coplanar waveguide resonators that are integrated with a single Josephson junction or, alternatively, a SQUID (Superconducting quantum interference device). This combined system is a real-time tunable nonlinear microwave resonator that is driven by an external magnetic field [14]. This tunable nonlinear microwave resonator can be parametrically pumped by applying a strong microwave signal close to the resonance frequency or twice its resonant frequency, depending on the mixing process.

In the following section, the theoretical aspects of the JPA, which constitute the core focus of this

thesis, will be delved into. As a starting point, nonlinear Kerr resonators will be explored, proceeded by the demonstration of the Four Wave Mixing mechanisms that are fundamental to amplification. The articles of Eichler et al. [15] and Splitthoff et al. [16] will be mostly benefited from, as the theory part is explained by them in a very effective and clear way. Next, the parameters of the amplifier will be investigated, and finally, in the conclusion, the components of the JPA design and the elements of its setup will be handled.

The resulting amplification is described using a general nonlinear resonator, commonly referred to as a Kerr resonator, without the analysis initially being restricted to a specific implementation. The Hamiltonian of a Kerr resonator, with eigenfrequency ω_0 and Kerr coefficient K, is given by:

$$H_{\text{JPA}} = \hbar\omega_0 a^\dagger a + \frac{\hbar K}{2}(a^\dagger)^2(a)^2 \tag{5}$$

where $a^\dagger$ and a are the raising and lowering operators that describe the intra-cavity field. The Kerr coefficient K in a Hamiltonian superconducting parametric amplifier Hamiltonian quantifies the strength of the nonlinear interaction. Furthermore, it originates from the intrinsic nonlinear properties of the superconducting material.

By substituting the Hamiltonian from Equation 5 into the Liouville–von Neumann equation and applying the commutation relation $[a, a^\dagger] = 1$, the intra-cavity field a of the resonator can be described as:

$$\frac{\partial a}{\partial t} = -i\omega_0 a - iKa^\dagger(a)^2 - \frac{\kappa+\gamma}{2}a + \sqrt{\kappa}a_{\text{in}} + \sqrt{\gamma}b_{\text{in}} \tag{6}$$

which is a Lindblad equation. It incorporates driving fields and interaction with the environment [17]. The isolated quantum system's unitary evolution is represented by the first two terms on the right. The additional terms, manually included, represent the driven, dissipative, non-unitary evolution resulting from the system's interaction with the environment. The coefficients κ and γ measure the coupling strength to a coherent mode, which, in this case, is the transmission line with input and output fields $a_{\text{in/out}}$ and all other loss channels $b_{\text{in/out}}$.

The input-output relation for a resonator coupled to a coherent mode is given by:

$$a_{\text{out}} = \sqrt{\kappa}a - a_{\text{in}} \tag{7}$$

To solve for the differential equation, the following ansatz is used:

$$a \to (a+\alpha)e^{-i\omega_p t}, \quad a_{\text{in}} \to (a_{\text{in}}+\alpha_{\text{in}})e^{-i\omega_p t}, \quad a_{\text{out}} \to (a_{\text{out}}+\alpha_{\text{out}})e^{-i\omega_p t} \tag{8}$$

The superposition of the quantum field a and the classical field α rotating at the pump frequency ω_p, hence $e^{-i\omega_p t}$, are used to account for the coherent drive field and the signal field. After putting the ansatz into the Equation 6 and grouping the terms with only classical fields, the steady-state response ($\dot{\alpha} = 0$) is given by:

$$\left(-i(\omega_p - \omega_0) + \frac{\kappa+\gamma}{2}\right)\alpha + iK\alpha^*\alpha^2 = \sqrt{\kappa}\alpha_{\text{in}} \tag{9}$$

When it is written in terms of its new quantities :

$$\left(-i\delta + \frac{1}{2} + i\xi n\right)\alpha = \tilde{\alpha}_{\text{in}} \tag{10}$$

$$\delta \equiv \frac{\omega_p - \tilde{\omega_0}}{\kappa+\gamma}, \quad \tilde{\alpha}_{\text{in}} \equiv \frac{\sqrt{\kappa}\alpha_{\text{in}}}{\kappa+\gamma}, \quad \xi \equiv \frac{|\tilde{\alpha}_{\text{in}}|^2 K}{\kappa+\gamma}, \quad n \equiv \frac{|\alpha|^2}{|\tilde{\alpha}_{\text{in}}|^2} \tag{11}$$

In Equation 11, the dimensionless drive amplitude is represented by $\tilde{\alpha}_{\text{in}}$, the product of drive power and nonlinearity, ξ is also expressed in dimensionless units, and δ is the detuning between the pump and resonator frequency in units of the total resonator linewidth. Lastly, with respect to the incident pump power, n is the mean number of pump photons in the resonator relative to the incident pump power.

When it is multiplied with its complex conjugate, Equation 12 can be obtained:

$$\left(\delta^2 + \frac{1}{4}\right) n + 2\xi\delta n^2 + \xi^2 n^3 = 1 \tag{12}$$

It is possible to solve Equation 12, a cubic equation in n, analytically. An explicit analytical expression for n in terms of δ and ξ is assumed, and the long solutions are omitted. In Figure 5 shows n as a function of δ for ξ in various ξ_{critic} levels. It can be seen that the maximum resonator occupancy is always 4; the conditions that maximize the performance of the amplification process are called optimal pump conditions. This specific set of parameters for the pump signal has a relationship between δ and ξ, which is $\delta = 4\xi$.

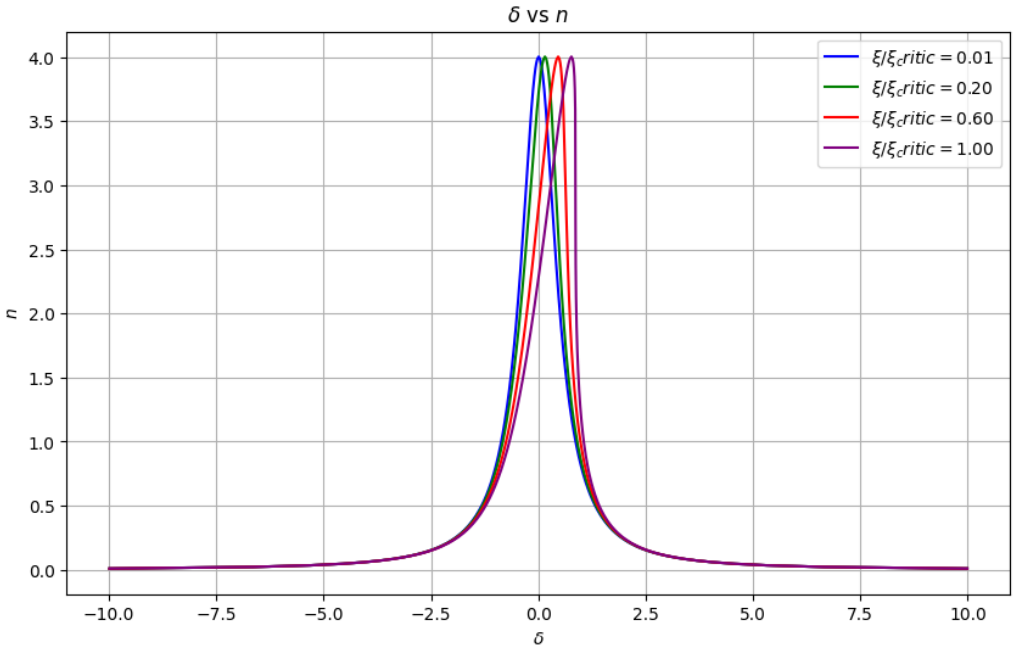

Figure 5: Mean photon number in the resonator n vs. detuning between the resonator frequency and the pump frequency δ for different driven strengths ξ

Moreover, one of the important points that can be drawn from Equation 12 is that the cubic equation has critical points in Equation 13 derived from $\frac{d}{dn} = 0$. It is helpful to find the delta criterion δ_{c}, which provides information about the system's regime limits depending on the critical n value. The system has only one critical point, which guarantees that the system operates in the parametric regime when it is above the δ_{c} which equals to $-\frac{\sqrt{3}}{2}$, otherwise the system may operate in the bifurcation regime, which is the different regime since n has two roots. Another critical value is for the ξ. The derivative $\partial n/\partial\delta$ diverges at the critical value $\xi_{\text{crit}} = -1/\sqrt{27}$, making the parametric amplifier extremely sensitive to small perturbations.

$$n_c = -\frac{2\delta}{3\xi} \pm \frac{1}{3\xi}\sqrt{\delta^2 - \frac{3}{4}} \tag{13}$$

Taking into account these critical points, the operating point of a parametric amplifier is set by the power of the pump field, the system's nonlinearity, and the δ value.

Finally, the complex reflection coefficient (Γ) is measured in order to determine the system parameters. This reflection coefficient can be calculated by using Equation 10 and the input-output relation $\alpha_{\text{out}} = \sqrt{\kappa}\alpha - \alpha_{\text{in}}$:

$$\Gamma = \frac{\alpha_{\text{out}}}{\alpha_{\text{in}}} = \frac{\sqrt{\kappa}\alpha}{\alpha_{\text{in}}} - 1 = \frac{\kappa}{\kappa + \gamma}\left(\frac{1}{-i\delta + \frac{1}{2} + i\xi n} - 1\right) \tag{14}$$

For zero loss $\gamma = 0$, the magnitude Γ equals to 1. All coherent power is transferred into the loss modes at resonance at critical coupling ($\gamma = \kappa$). However, the most significant information derived from this reflection coefficient is in regard to the design of the phase-matching condition. Specifically, the amplification process that could occur in an optical system or a Josephson Traveling Wave parametric amplifier must satisfy the phase-matching condition. For example, to maximize gain and bandwidth, the JTWPA design uses a sequence of linear lumped-element resonators, one of the different resonant phase-matching techniques [12]. However, this condition is automatically satisfied in the JPA by using only the resonator. This can only be observed by examining the reflection, or in other words, the phase of the S11 parameter, and with this information, resonance frequency in which JPA operates can be determined, as will explored in Chapter 2.

1.2.1 Four Wave Mixing

This section introduces the concept of Four-Wave Mixing (FWM), which forms the basis of the amplification theory in JPAs. It is a nonlinear process in which interactions between four waves produce new results in the amplification of certain signals.

To understand the amplification mechanism, the dynamics of a nonlinear Kerr resonator must be considered. By incorporating the appropriate ansatz in Equation 8 into the Lindblad equation, the following expression is derived:

$$\frac{\partial a}{\partial t} = i\left(\omega_p - \tilde{\omega_0} - 2K|\alpha|^2 + i\kappa + \frac{\gamma}{2}\right)a(t) - iK\alpha^2 a^\dagger(t) + \sqrt{\kappa}a_{\text{in}}(t) + \sqrt{\gamma}b_{\text{in}}(t). \tag{15}$$

This equation describes the time evolution of the mode $a(t)$, where ω_p is the pump frequency, K is the Kerr nonlinearity coefficient, κ represents the coupling rate, γ is the loss rate, and α is the coherent pump amplitude. The terms $a_{\text{in}}(t)$ and $b_{\text{in}}(t)$ represent the input fields. Since the quantum field a is a weak signal, this equation is in a reduced form. The parts containing its high orders, such as a^2 and a^3 can be easily neglected. The terms involving the Kerr coefficient (K) facilitate the four-wave mixing process.

To solve Equation 15, first, all modes including a_{in} and b_{in} are decomposed into their Fourier components:

$$a(t) \equiv \sqrt{\frac{\kappa + \gamma}{2\pi}} \int_{-\infty}^{\infty} e^{-i\Delta(\kappa+\gamma)t} a_\Delta \, d\Delta \tag{16}$$

Δ in Equation 16 is the detuning between the pump and signal frequencies, being expressed in the linewidth as $\kappa + \gamma$.

By substituting the Fourier decomposition into Equation 15 and comparing the coefficients of different harmonics, one gets:

$$0 = \left[i(\delta - 2\xi n + \Delta) - \frac{1}{2} \right] a_\Delta - i\xi n e^{2i\phi} a^\dagger_{-\Delta} + \tilde{c}_{\text{in},\Delta} \tag{17}$$

where

$$\tilde{c}_{\text{in},\Delta} \equiv \frac{\sqrt{\kappa} a_{\text{in},\Delta} + \sqrt{\gamma} b_{\text{in},\Delta}}{\kappa + \gamma} \tag{18}$$

represents the sum of all field modes incident on the resonator. Here, (ϕ) is the phase of the intra-resonator pump field, defined by $(\alpha = |\alpha| e^{i\phi})$. The coupling between the modes (a_Δ) and $(a^\dagger_{-\Delta})$ in Equation 17 can be interpreted as a wave mixing process. It is rewritten as a matrix equation:

$$\begin{pmatrix} \tilde{c}_{\text{in},\Delta} \\ \tilde{c}^\dagger_{\text{in},-\Delta} \end{pmatrix} = \begin{pmatrix} i(-\delta + 2\xi n + \Delta) + \frac{1}{2} & i\xi n e^{2i\phi} \\ -i\xi n e^{-2i\phi} & i(\delta - 2\xi n - \Delta) + \frac{1}{2} \end{pmatrix} \begin{pmatrix} a_\Delta \\ a^\dagger_{-\Delta} \end{pmatrix}.$$

While the signal field oscillates at a frequency Δ around the pump field, the conjugate field, known as the idler field, oscillates at $-\Delta$. Thus, the frequency of the idler tone is given by $\omega_I = 2\omega_P - \omega_S$. By inverting the matrix on the right-hand side, the intra-resonator field a can be expressed in terms of the incoming field $(\tilde{c}_{\text{in},\Delta})$:

$$a_\Delta = \frac{i(\delta - 2\xi n - \Delta) + \frac{1}{2}}{(i\Delta - \lambda_-)(i\Delta - \lambda_+)} \tilde{c}_{\text{in},\Delta} + \frac{-i\xi n e^{2i\phi}}{(i\Delta - \lambda_-)(i\Delta - \lambda_+)} \tilde{c}^\dagger_{\text{in},-\Delta} \tag{19}$$

where $\lambda_\pm = \frac{1}{2} \pm \sqrt{(\xi n)^2 - (\delta - 2\xi n)^2}$.

Using Equation 7, the final transformation between input and output modes is given by:

$$a_{\text{out},\Delta} = g_{S,\Delta} a_{\text{in},\Delta} + g_{I,\Delta} a^\dagger_{\text{in},-\Delta} + \frac{\gamma}{\kappa}(g_{S,\Delta} + 1) b_{\text{in},\Delta} + \frac{\gamma}{\kappa} g_{I,\Delta} b^\dagger_{\text{in},-\Delta}, \tag{20}$$

and in the zero loss limit $\gamma/\kappa \to 0$:

$$a_{\text{out}} = g_{S,\Delta} a_{\text{in},\Delta} + g_{I,\Delta} a^\dagger_{\text{in},-\Delta}, \tag{21}$$

where:

$$g_{S,\Delta} = -1 + \frac{\kappa}{\kappa + \gamma} \frac{i(\delta - 2\xi n - \Delta) + \frac{1}{2}}{(i\Delta - \lambda_-)(i\Delta - \lambda_+)}, \tag{22}$$

and

$$g_{I,\Delta} = \frac{\kappa}{\kappa + \gamma} \frac{-i\xi n e^{2i\phi}}{(i\Delta - \lambda_-)(i\Delta - \lambda_+)}. \tag{23}$$

This process can be comprehended as a pump photon splitting into an idler photon and a signal photon, ensuring that energy is conserved, $(2\omega_p = \omega_s + \omega_i)$ [14]. This process is called Four Wave Mixing(FWM).

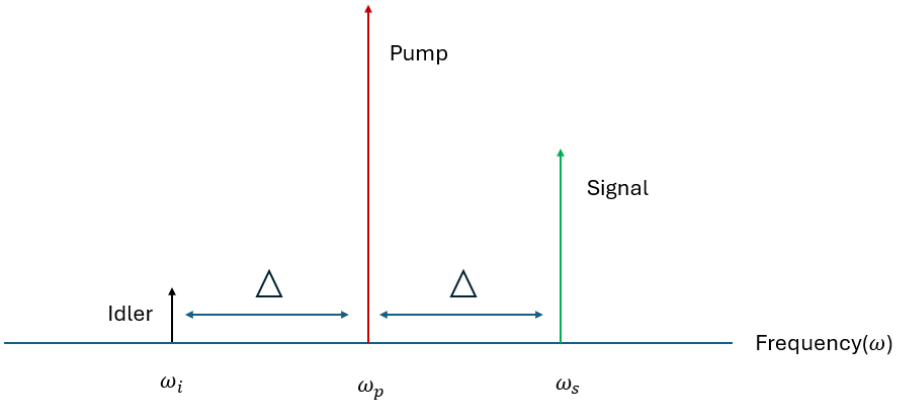

Figure 6: Four Wave Mixing Scheme

In Figure 6, the generation of new frequencies through nonlinear interactions in FWM directly can be seen in the frequency domain. The red signal is the pump signal that starts the FWM process. The green signal, at w_s, represents the amplified weak signal by the power gain $G = |g_{S,\Delta}|^2$, detuned by Δ from the pump and the black one is mixed with the idler signal at the w_p corresponding to minus detuning $(-\Delta)$ from the pump.

The quantity $g_{S,\Delta}$ in Equation 22 encapsulates the characteristic properties of the parametric amplifier, including the bandwidth and maximal gain. This function depends on detuning between the signal and pump field's frequencies, Δ, and effective drive strength.

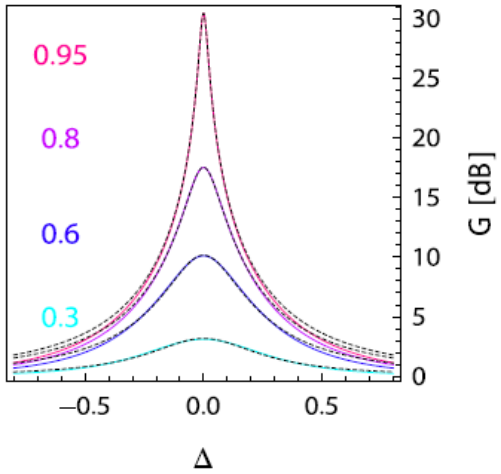

Figure 7: Gain vs. Δ for driven strengths ξ/ξ_{crit} and optimal pump detuning [15]

In Figure 7 adapted from Ref. [15], at the optimum driven strength, different gain plots in a Lorentzian shape can be obtained for different optimum delta values. When the Δ value is set to 0, it means that the signal and pump frequency are at the same spot, and the highest gain, G_0, can be achieved with the optimum δ value and the corresponding optimum ξ value. Moreover, the graph reveals an important insight into the relationship between gain and bandwidth. Namely, it can be inferred that the gain-bandwidth product (GBW or GBWP) -a key performance metric for amplifiers- is approximately 1 ($\sqrt{G_0}B \approx 1$). As it can be seen from the figure, the bandwidth, B, is related to the detuning Δ for

which the gain decreases by 3 dB. The delta is in units of resonator linewidth (κ+γ), and γ in this context is negligible, as it can be approximated to be close to zero, leading to the bandwidth directly depending on κ and, inversely, the square root of the gain. Therefore, in a parametric amplifier, boosting the gain by enhancing the pump strength results in a trade-off as the effective operating bandwidth decreases [18].

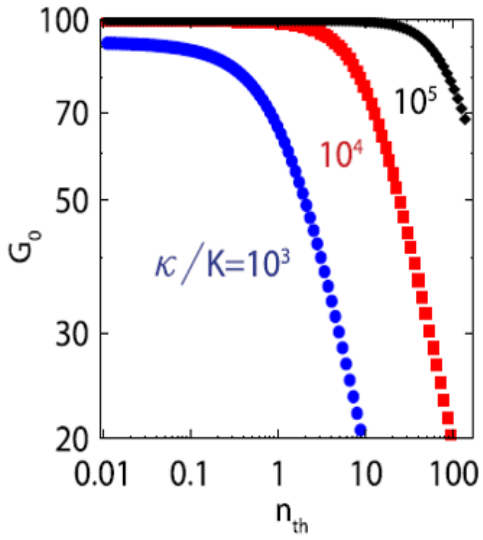

Figure 8: Gain vs. number of photon for different κ/K values [15]

The calculations made so far, and the gain equations obtained were valid for stiff approximation, where the pump signal is considered to be much higher than the quantum signal to be amplified. However, most of the time, when designing an amplifier, it is desired that this amplifier works not only for weak signals but also for high-power input signals. The increase in signal power results in a reduction of signal gain since this can eventually exhaust the supply of pump photons that provide the gain, which is called "pump depletion" [11]. This is logical because the amplifier gain is a highly sensitive function of the applied pump photon flux. Consequently, more pump photons are transformed into signal photons, leading to the gain decreases [19]. The mean-field approach is preferred in analyzing the pump depletion, and the terms in Equation 15 are not used in the analysis. Based on this model, we find that the gain from the stiff approximation drops when the signal strength exceeds a certain level; the range where the gain decreases by 1 dB is called the dynamical range. A 1 dB change represents approximately a 25% change in power, which is an acceptable change. It is desired to keep this dynamical range as high as possible, and the value generally depends on κ over K. Figure 8 adapted from Ref. [15], displays that the number of input photons (n_{th}) at which this happens becomes bigger with increasing ratio κ/K.

Another factor that can lower the dynamic range of an amplifier is vacuum fluctuations, which are always incident on all ports and occur even in the absence of an incident signal. This means that the pump cannot be considered perfectly stiff in a precise analysis. Increasing these vacuum fluctuations also decreases the device's dynamic range [20].

This effective Hamiltonian is obtained directly from the full circuit model of a $\frac{\lambda}{4}$ transmission line resonator, which is capacitively coupled to a transmission line and terminated at the short-circuited end by a SQUID loop. The nonlinearity of the resonator was studied in detail in Eichler's and Lukas's papers Reference [15, 16].

First, the starting point is the Hamiltonian of the resonator is

$$H = \sum_n \hbar\omega_n \left(a_n^\dagger a_n + \frac{1}{2}\right) + \sum_n \left(\hbar\frac{K_{nn}}{2}(a_n^\dagger a_n)^2\right) + \sum_{n,m\neq n} \left(\hbar\frac{K_{mn}}{2} a_m^\dagger a_m a_n^\dagger a_n\right) \tag{24}$$

Here, ω_n and K_{nn} represent the resonance frequency and self-Kerr coefficient of mode n, respectively. The terms proportional to K_{mn}, where $m \neq n$, are terms used in cross-Kerr interactions that couple various modes to one another, while a_n ($a_n^\dagger$) are the annihilation (creation) operators for the intra-resonator field of mode n. However, only K_{00} which characterizes the fundamental mode's Kerr nonlinearity, is used in the parametric amplification procedure [21].

$$K_{00} = \frac{\hbar L_r \cdot \cos^4(k_0 d)}{C_r \cdot (k_0 d)^2 \cdot \left(\left(1 + \frac{\sin(2\cdot k_0 d}{2\cdot k_0 d}\right)^2 \cdot (4 \times 10^{-30}) \cdot L_J\right)} \tag{25}$$

with:

$$k_0 \approx \frac{\pi}{2d(1 + \frac{L_J}{L_r})} \tag{26}$$

In the Equation 25, K_{00} formula can be seen. d represents the length of the resonator, and the quantity (k_0) characterizes the valid wave vector of the fundamental mode, which is established by the boundary conditions at both ends of the ($\lambda/4$) transmission line in equations 25 and 26. When the value for k_0 in Equation 26 is inserted into 25, the following equation can be obtained:

$$K_{00} = \frac{\hbar L_r \cdot \cos^4(\frac{\pi \cdot L_r}{L_r + L_J})}{4 \times 10^{-30} \cdot C_r \left(\left(1 + \frac{\sin(\frac{2\pi \cdot L_r}{L_r + L_J})}{L_r + L_J}\right)^2 \cdot L_J\right)} \tag{27}$$

Specifically, it depends on the physical parameters of the resonator(L_r,C_r) and junction(L_J). The effect of $\cos^4$ and $\sin^2$ terms makes the Kerr nonlinearity K_{00} highly sensitive to the physical parameters of the resonator and junction. Therefore, K_{00} encapsulates the complex interplay of these elements.

Other important point is noise contribution of the amplifier. The signal coming from the fluxonium readout resonator is around -160 dBm.To strongly amplify such a low signal, amplifiers with high gain and bandwidth compared to JPAs, such as HEMT, could be used at 4 K. However, such amplifiers would have a major problem, especially at cryogenic temperatures. They introduce significantly more noise into the system, and if this noise is added in the first step of the amplification process, as seen in the following, it can reach very high levels that can reduce the SNR. To realize this, it is necessary to use structures that will add very low noise at these temperatures. Therefore, it is advantageous to place the JPA to optimize the overall system performance. This placement minimizes the system's noise figure, leveraging the JPA's low noise contribution at the initial amplification stage.

There is a lower bound on the additional noise that results from the amplification process itself; this lower bound or fundamental limit is known as the quantum limit. Specifically, a well-designed JPA can achieve a noise temperature close to the quantum limit of half a photon at the operating frequency, significantly lower than classical amplifiers. The quantum limit of the noise temperature T_Q is given by:

$$\frac{hf}{2k_B} \tag{28}$$

In the Equation 28, f represents the frequency, k_B is the Boltzmann constant, and h is the Planck constant. To give an example of how quite small this value is, a quantum noise equivalent to 0.240 K is obtained at 10 GHz. For Yamamato's article HEMT, the noise temperature at 10GHz is approximately 9K [22]. Hence, a JPA operating near this limit would have an exceptionally low noise temperature.

The impact of this configuration can be quantitatively understood using the Friis formula for noise, which is given by:

$$T_{\text{total}} = T_1 + \frac{T_2}{G_1} + \frac{T_3}{G_1 G_2} + \cdots$$

where T_{total} is the total noise factor, the (i)-th stage's gain is called (G_i), and its noise factor is called (T_i). The noise factor is a measure of the noise power within a system, expressed in terms of the temperature that would generate the same amount of thermal noise power.

Placing the JPA, which has a noise factor close to quantum-limited noise, at the first stage (T_1), and a HEMT amplifier, which typically has a higher noise factor, at the second stage, the overall noise figure is minimized because the low noise figure of the JPA dominates the term (T_2), and the noise contribution of subsequent stages is divided by the high gain (G_1) of the JPA.

1.2.2 Components of JPA

After investigating how the parametric amplifiers work and analyzing the important features of the parametric amplifier, the components that make up a parametric amplifier can be described.

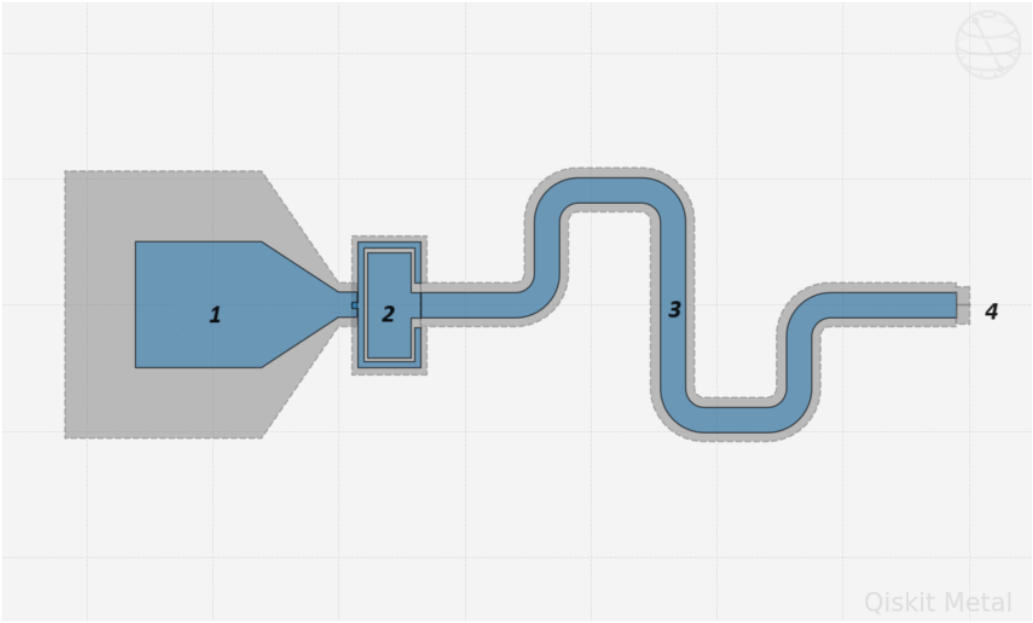

Figure 9: Four different parts of the JPA: (1) Launchpad, (2) T-coupler, (3) CPW resonator, (4) SQUID junction

Figure 9 shows four different components of the parametric amplifier, which have different functions. The four parts were designed separately in Qiskit metal, a specialized framework for quantum device engineering, and they are integrated with the appropriate commands.

The design's first part is a launchpad that interfaces the superconducting circuit and external mea-

surement and control equipment.

In the second part, a Josephson amplifier design uses a T-coupler to connect the amplifier to external circuitry in the setup capacitively. It is typically employed to set the coupling strength or linewidth(κ), which mostly depends on the gap distance in the coupler.

The linewidth (κ) in the context of superconducting circuits refers to the decay rate of the resonator mode, which is related to the coupling quality factor (Q).It is directly proportional to the resonator frequency and inversely proportional to the κ value. Stronger coupling (through the T-coupler) increases the decay rate (κ), leading to a broader linewidth; this results in a low-quality factor. This is desirable for JPA circuits because it indicates how quickly energy is returned rather than stored, unlike qubit systems where the opposite is desired.

The third part is the resonator section; many different types of transmission lines could be chosen for this part. In the design, the use of the Coplanar Waveguide (CPW) resonator was chosen for several important reasons. The important reason of this is that in a CPW, the center conductor and the two ground planes are printed on the same surface of a dielectric substrate. This configuration confines predominantly the fields to the plane of the substrate. For example, microstrip lines have a ground plane on the opposite side of the dielectric, leading to more extensive field spreading and potentially higher radiation losses. This tighter field confinement in CPWs reduces parasitic effects, such as unwanted coupling and leakage [23]. Another reason is the integration of nonlinear elements like Josephson junctions on which parametric amplifiers rely. CPWs provide a more flexible and accessible platform for integrating these elements. Since all conductive surfaces in a CPW are on the same plane, it is easier to place and connect nonlinear components precisely where the electromagnetic field intensity is highest [24].

CPW transmission lines can be analyzed using either a lumped or distributed element. When the circuit length is similar to or way smaller than the wavelength, lumped element components such as capacitor, inductor, and resistor are used to represent the electrically smaller sections of the transmission line. This model is called the "Lumped element model." In these instances, the circuit parameters are considered independent of frequency. However, wave equations are necessary for RF or higher frequencies circuit analysis. Since the working range is between 4 and 8GHz, the size of our circuit, between 1 and 4 millimeters in length, will be larger than the wavelength. at these high frequencies, distributed element models are suitable for employing microscale circuits [25].

In the distributed element method for analyzing transmission lines, the transmission lines can be approximated as 'lossless' transmission lines with a characteristic impedance given by ($Z = \sqrt{L_0/C_0}$), where L_0 and C_0 represent the inductance and capacitance per unit length of the transmission line, respectively as our CPW structures are made of superconducting material. These distributed parameters, L_0 and C_0, are used in the telegrapher's equations derived from Maxwell's equations to describe voltage and current behavior at high frequencies.

To create a resonant structure, boundary conditions must be applied to the waves propagating through the transmission line. Since the focus in the design is on quarter-wavelength resonators, a discontinuity in the transmission line with a coupling capacitance (T-coupler fulfills) can be introduced, and the CPW can be made to short-circuit to the ground as shown in Figure 10 adapted from Ref. [14].

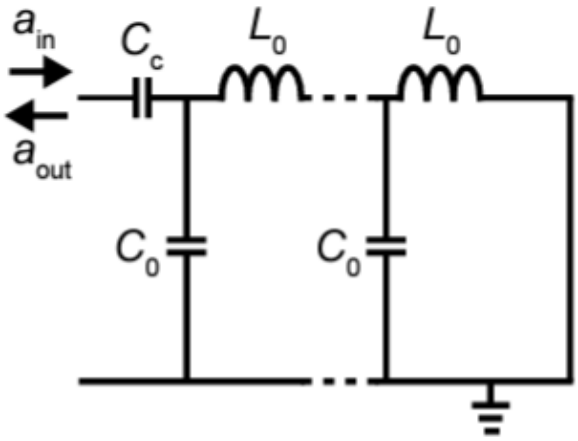

Figure 10: Distributed element model of quarter-wave resonator [14]

The fundamental resonance frequency of a quarter-wavelength resonator with length l is given by:

$$f_r = \frac{c}{\sqrt{\epsilon_{\text{eff}}}} \cdot \frac{1}{4l} = \frac{1}{4l\sqrt{L_0 C_0}} \tag{29}$$

where ($\epsilon_{\text{eff}} = \frac{c^2}{v_{\text{ph}}^2}$) is the effective permittivity of the CPW, c is the speed of light in vacuum, and $v_{\text{ph}} = \frac{1}{\sqrt{L_0 C_0}}$ is the phase velocity.

The Equation 29 mentioned here is based on the fundamental principles of LC circuits, where the total capacitance and inductance of the circuit determine the resonant frequency. The resonator itself has the maximum impact on the frequency. Moreover, our interest lies only in fundamental modes (when j equals zero) rather than higher harmonics in the resonator. The fundamental mode often allows for maximal energy storage with minimal losses. Hence, higher modes try to avoid this range because it typically corresponds to more complex field distributions that can lead to increased radiation losses or energy dissipation through other mechanisms, such as dielectric losses or coupling to external modes.

The last part used in the JPA design is the nonlinear element as SQUID, which consists of two Josephson junctions in a superconducting loop. It can be precisely tuned by an external magnetic flux. However, in the designed circuit, the magnetic flux is static so that the inductance of the junction is adjusted to 1 nH. Therefore, the only part that should be taken into account for changing the inductance in the nonlinear element is the pump current. The pump current can modulate the inductance as in Equation 30.

$$L \approx L_J \left(1 + \frac{1}{6}\left(\frac{I(t)}{I_C}\right)^2\right) \tag{30}$$

Any increase in the inductance increases the Kerr coefficient as it can be seen in Equation 27. This directly affects the amplifier's dynamic range and can also shift the resonance frequency of the amplifier.

1.2.3 Setup

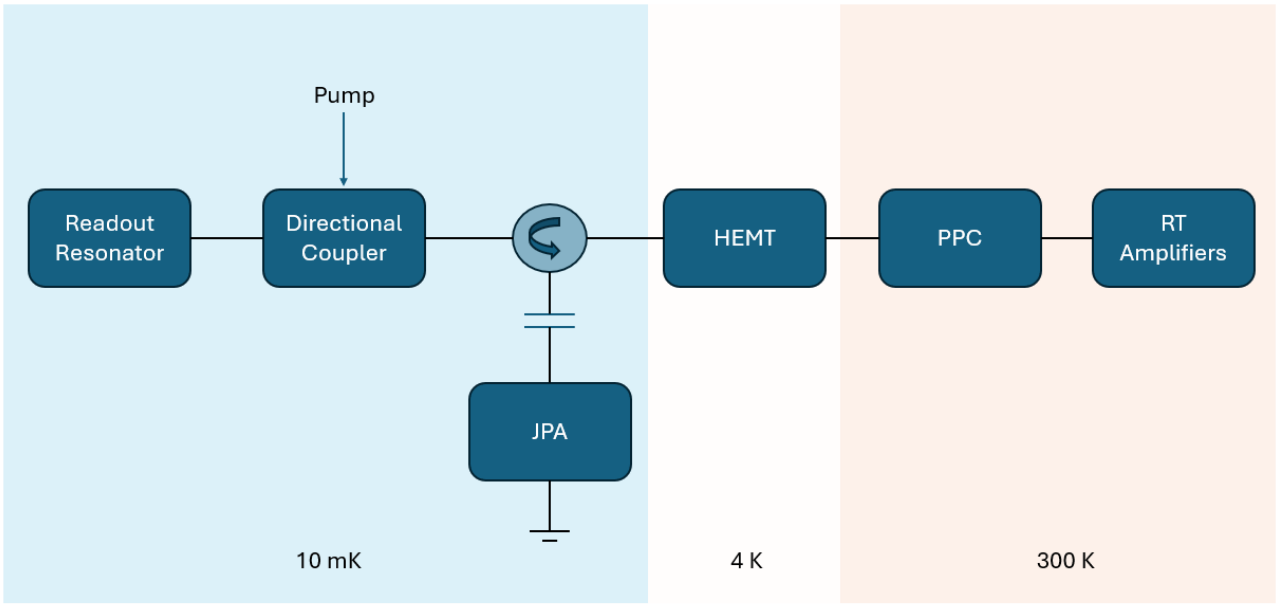

Figure 11: Amplification Chain from the fluxonium qubit readout resonator to the room temperature electronics

In Figure 11, a schematic of the amplification process for a signal originating from a fluxonium qubit is presented. The process begins with a weak readout signal passing through a directional coupler.

The directional coupler, depicted in the Figure 12 above, is a four-port waveguide. It comprises a primary waveguide (ports 1 and 2) and a secondary waveguide (ports 3 and 4). In this configuration, the signal coming from the fluxonium readout resonator passes from port 1 to port 2, and since it is coupled with the secondary waveguide, 40dB less signal reaches port 3. However, since this signal is weak, the signal going to this port is unimportant. The main effect is the pump signal coming from port 3. This signal passes to port 2 and port 1. Switching to port 2 decreases by 20 dB, and when switching to port 1, it decreases by 40 dB. Since the pump signal is strong, the signal passing to port 1 can be eliminated with the help of an isolator. As a result, it is obtained by combining our readout signal and our new pump signal in port 2. The only problem is, as seen in the theory part, it is necessary to compensate for this decrease in the power of the pump signal, otherwise, this will directly affect our drive strength ξ.

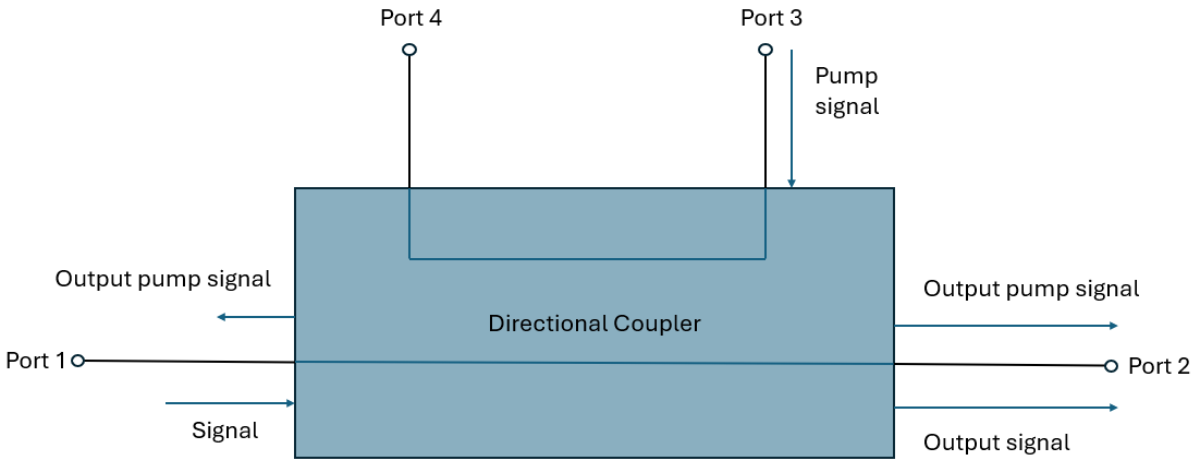

Figure 12: Power Combining Directional Coupler

The next step is the circulator, which is a non-reciprocal device that allows the transmission of electromagnetic signals in one direction while blocking them in the opposite direction. It has three ports, where the signal enters one port, exits the next port in a specified rotational order, and is isolated from the remaining ports [26, 27]. This combined signal is then directed to the parametric amplifier, initiating the amplification process.

Following the initial amplification by the parametric amplifier, as covered in the theoretical part, the incoming pump changes the nonlinear inductance of the SQUID, allowing the weak signal to be amplified up to 20dB, which is its maximum limit. After this, the signal undergoes two further amplification stages. The first of these is the High Electron Mobility Transistor (HEMT) amplifier, which operates at cryogenic temperatures around 4K. This cryogenic amplifier significantly amplifies the signal 40 dB before it reaches the second amplification stage at room temperature. The room temperature (RT) amplifier then further amplifies the signal for subsequent processing. In addition to that, the HEMT has a significant impact on the frequency range of the amplifier and the readout resonator, limiting it to the operating range of the readout resonator and JPA to 4-8 GHz.

However, an issue arises as the HEMT amplifier can amplify the pump signal to such an extent that it saturates the RT amplifier, negatively impacting the readout fidelity of the signal. To address this problem, various techniques, such as using low-pass filters or attenuators, can be employed. However, the pump tone and the amplified signal are really close to each other in the frequency domain, approximately only 5MHz, which makes it difficult to use a filter solution. The most effective solution is to utilize destructive interference via a programmable parametric pump controller (PPC), effectively suppressing the pump signal. The basic principle of PPC is based on the destructive interference of the pump signal with a canceling signal, which has the same frequency as the pump but a 180-degree phase difference.

In the final stage of the amplification process, room temperature amplifiers boost the signal to the desired level, preparing it for subsequent demodulation and detection. This comprehensive amplification chain ensures that the weak initial signal is obtained with high gain and high SNR for accurate readout and analysis.

2 Design of Josephson Parametric Amplifiers

This chapter focuses on the design approach for Josephson parametric amplifiers. First, in Section 2.1, important design parameters and goals related to Kappa and Kerr values are identified. Next, the software tools used in the design process, specifically COMSOL and Microwave Office, along with their working principles, are introduced in Section 2.2. In Section 2.3, the methodology and the design process are detailed. Finally, in Section 2.4 the final outcomes of the simulations are presented.

2.1 Parameter Target

As mentioned before, quantum information as reached photons of microwave radiation from fluxonium qubit, being in the band between 4-8 GHz [4], has a small energy. It is barely possible to detect and process this signal. It is particularly necessary to design a Josephson parametric amplifier apt for this need, which is optimized to operate at this frequency.

These amplifiers have limited dynamic range and narrowband gain. In this design, to avoid these disadvantages, the target parameter kappa value was chosen as 100 MHz and the Kerr coefficient value as 1000 Hz, which ensures precise and efficient amplification of these microwave signals.

The desired readout generally is in 100 ns [1], corresponding to 10 MHz, the readout pulse bandwidth. Hence, the JPA bandwidth must be much higher than this value. For this reason, the first target parameter for the linewidth (κ) of 100 MHz was chosen to balance the need for fast readout and signal integrity. A 100 MHz linewidth allows for rapid detection of the fluxonium qubit signal, enabling high-speed data acquisition and processing while maintaining a reasonable noise floor. This bandwidth is wide enough to promptly capture the signal and preserve the integrity of quantum information. On the other hand, the Kerr coefficient of approximately 1000 Hz was selected to provide controlled nonlinearity, which is crucial for enhancing certain quantum operations such as squeezing and frequency conversion without introducing instability. This moderate level of nonlinearity ensures manageable frequency shifts and allows for enough dynamic range for the readout signal with the large number of photons.

2.2 Computer Aided Design Approach

The design of Josephson Parametric Amplifiers (JPAs) relies heavily on computer-aided design (CAD) tools to tackle the challenges associated with superconducting circuits that operate at quantum mechanical levels. CAD tools enable the simulation of the amplifier's nonlinear dynamics, providing insights into the effects of critical currents, capacitance, and inductance on the amplifier's performance. This step is vital for the device's functionality, initial design, and theoretical underpinning. This project uses two simulation programs. One of them is COMSOL, powerful software that enables the modeling and simulation of complex physical processes across multiple physics domains. The software is widely recognized for its ability to handle coupled or multiphysics scenarios where interactions of different physical phenomena can be modeled. We calculate the capacitance matrix and display electric potential, showing the distribution of electric fields. Another program we used is Microwave Office, a software suite developed by Cadence Design Systems specifically tailored for designing and simulating microwave and RF (radio frequency) circuits. It is really helpful for calculating the amplifier's frequency and S_{11} parameters.

2.2.1 Finite Element Simulations

The core point of all these simulation programs is to make use of finite element simulation. Finite element simulation (FES) is a crucial computational technique used extensively in engineering and science to predict how objects and systems behave under various conditions. It starts with discretizing the domain of interest into a mesh of simpler, smaller elements connected at nodes, allowing the complex geometry and diverse material properties to be modeled accurately. Each element is assigned relevant physical properties and governed by specific equations reflecting the underlying physics of the problem. These local equations are then assembled into a comprehensive global system that integrates the interactions across all elements. Real-world boundary conditions are applied, and the resulting system of equations is solved numerically to find variables like electric field magnitude. The outcome is analyzed through graphical visualizations, providing insights that are pivotal for optimizing designs before physical prototypes are constructed.

2.3 Final Amplifier Design

2.3.1 Methodology

The design process methodologically consists of two parts. Figure 13 illustrates the steps of the first part involved in this method. It begins with designing the initial amplifier in Qiskit Metal, a tool that helps us design superconducting circuits. Following this, the Microwave Office is used to determine the magnitude and phase part of the reflection coefficient (S_{11}) of the amplifier. The phase part allows us to easily obtain the resonant frequency of the amplifier. After that, this reflection coefficient data is fitted in the developed code and helps find the resonator linewidth (κ). These steps are repeated iteratively until the frequency and coupling rate (κ) are adjusted to the desired value.

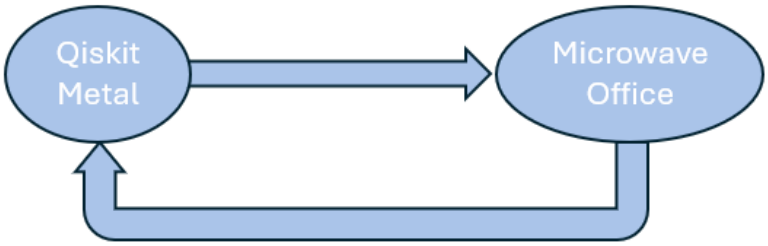

Figure 13: First step of the design process

Once the desired κ is achieved, the process moves to the second step, as illustrated in Figure 14. In this step, the design is imported into COMSOL Multiphysics to determine the Maxwell capacitance matrix. Subsequently, the Microwave Office is utilized again to achieve the resonant frequency. With both the capacitance and frequency determined, the inductance can be easily calculated using Equation 29. The Kerr value is then practically calculated using Equation 27. This iterative process continues, with the design being checked and refined. Once the desired Kerr value is reached, both the frequency and κ

values are verified in Microwave Office. If necessary, the process returns to step 1. This cycle repeats until the design is fully optimized.

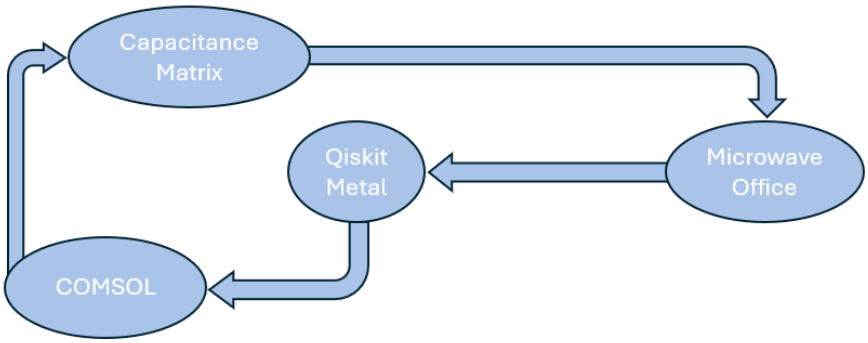

Figure 14: Second step of the design process

2.3.2 Design Process

This project has four Josephson Parametric Amplifier designs to receive readout signals with different frequencies between 4 and 8 GHz. Our primary focus in this part is on the design process of an amplifier operating at 8 GHz, which provides a promising baseline for exploring the impact of parameters and informing subsequent designs running at other frequencies.

To develop the design methodology, we begin by analyzing the targeted parameters of Step 1 and Step 2. This gives a preliminary understanding of how the various changes in the elements of the amplifier impact the targeted parameters such as frequency, κ, and Kerr coefficient.

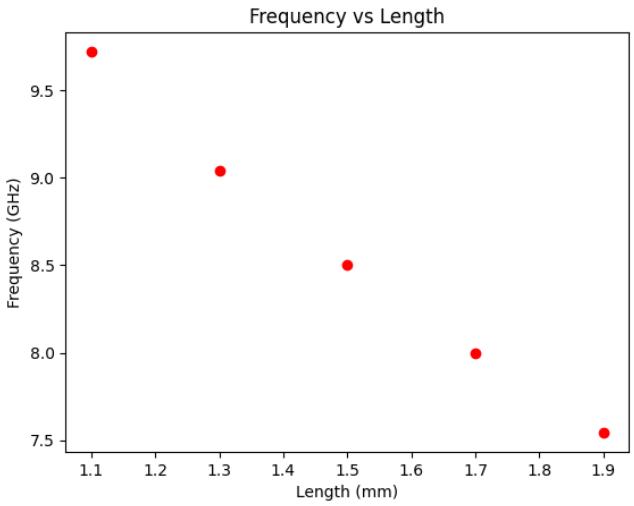

Figure 15: Relation of frequency with the length of the resonator

In Step 1, the first targeted parameter being analyzed is the amplifier's resonance frequency. It is an important parameter for the amplification process because it needs to be equal to the frequency of the pump signal. Otherwise, the gain can decrease due to the off-resonance. Therefore, in the initial design, parameters will be set to adjust the frequency to approximately 8 GHz.

One of the important parameters that we can analyze for frequency is length. As shown in Figure 15, when the length of the resonator increased from 1.1 mm to 1.9 mm, it is evident that the resonator's length influences the frequency significantly, and frequency rises, even when small changes are made to it. This is to be expected since the length is inversely proportional to the resonator frequency, as seen in Equation 29. The chosen initial length for the resonator is 1.7 mm, corresponding to 8 GHz as displayed in Figure 15.

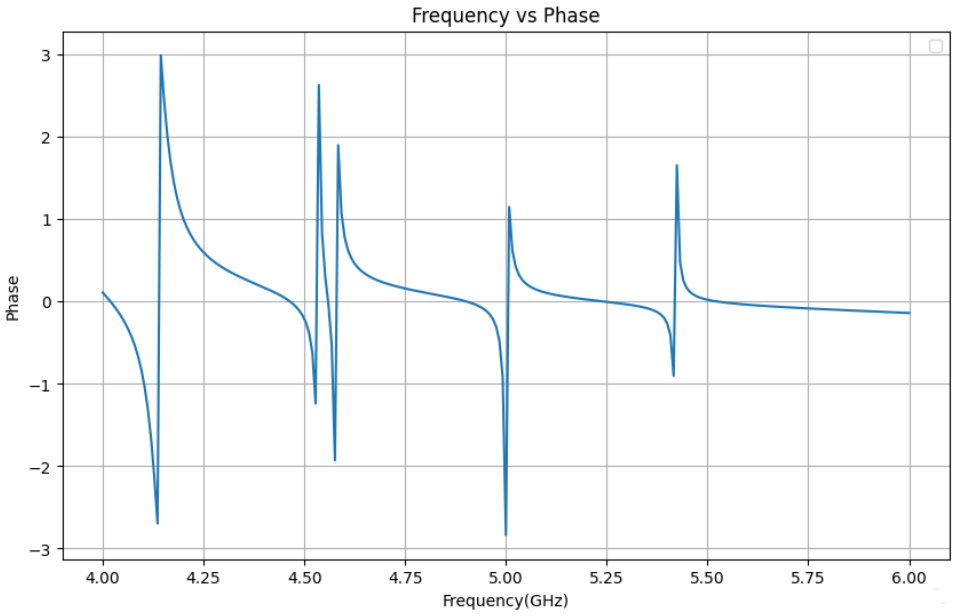

Figure 16: Phase vs. frequency graph for the amplifier with high inductance SQUID element

We need to mention that an intriguing observation has arisen. Although only a graph for five different length values is shown, during the design process, the length is also adjusted to long lengths for testing purposes. When the resonator is much longer, generating higher modes that fall within the desired frequency range, as shown in Figure 16, which is mentioned in the CPW part. These higher modes can couple to external systems, such as the feedline, as effectively as the fundamental mode, resulting in unwanted effects and a loss of energy intended for signal transmission. To mitigate this, the simulation emphasizes moving these modes out of range. Another factor contributing to these modes is the inductance of the inductive element, which should range between picoHenry (pH) and nanoHenry (nH). For large inductance values, changes in length become ineffective, and the higher mode becomes irreversibly dominant within the range used for fluxonium readout.

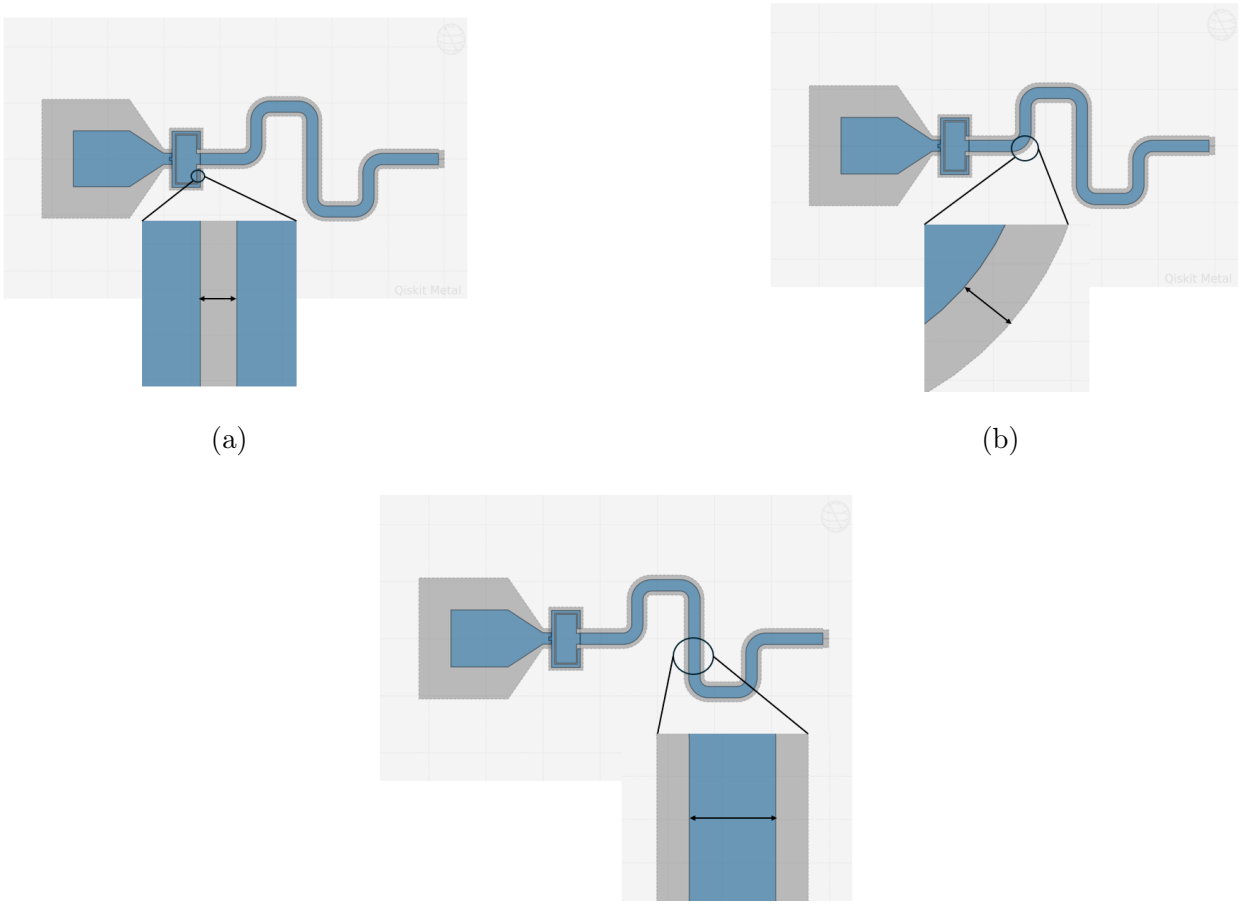

(a) (b)

(c)

Figure 17: Representation of JPA parameters on the circuit

In the subsequent sections, we will explore additional key parameters of the design, including the length and their impacts. These parameters, which directly influence the capacitance and inductance values of the amplifier, are crucial for fine-tuning the resonance frequency, κ, and Kerr coefficient. Figure 17 (a) illustrates the first parameter, the coupler gap distance. The resonator gap distance is the second parameter shown in Figure 17 (b). Lastly, the width of the resonator is depicted in Figure 17 (c).

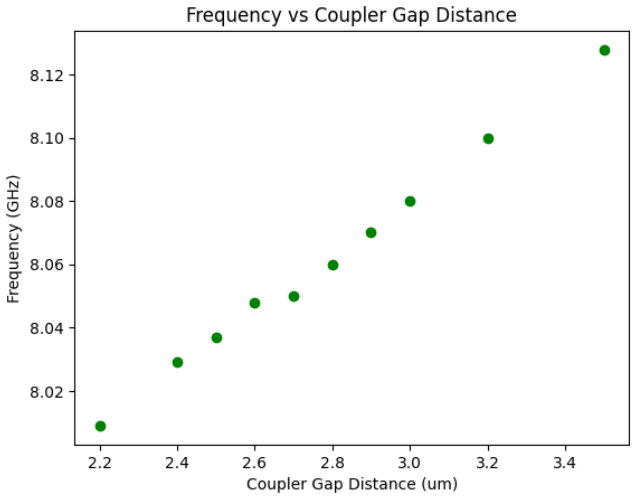

Figure 18: Relation of frequency with the coupler gap distance

When analyzing the relationship between the gap distance of the coupler in superconducting circuits and the resulting frequency changes, the data in Figure 18 obtained shows a subtle but noticeable variation in frequency as the gap distance increases. Specifically, the gap distance of the coupler was varied from 2.2 um to 3.4 um. Over this range, the frequency slightly decreased from 8.01 GHz to 8.13 GHz. The observed behavior is likely the result of alterations in the coupling strength within the coupler, where a larger gap likely reduces the coupling efficiency, thus impacting the resonant frequency.

The analysis used a 2 um gap distance in the initial design. The fact that it has a small effect on the frequency made me use the coupling distance in the design process when I needed to make small changes to the frequency.

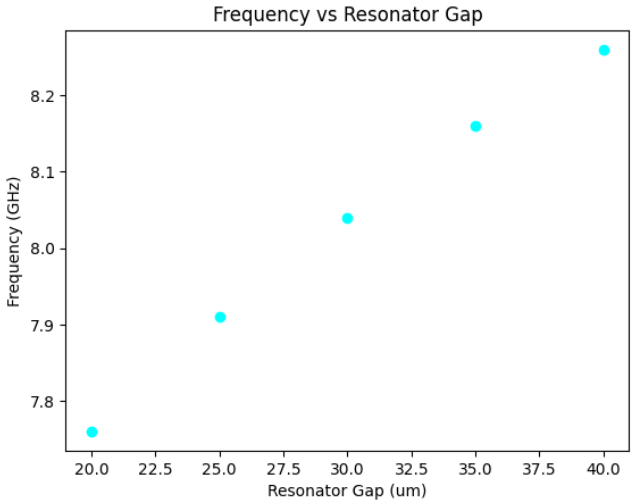

Figure 19: Relation of frequency with the resonator gap distance

Contrary to the coupler's behavior, increasing the gap of the resonator from 20 µm to 40 µm resulted in an increase in the resonant frequency, from 7.7 GHz to 8.3 GHz in Figure 19. A larger gap in the resonator reduces the capacitive effects while possibly increasing the inductive pathways. Hence, this could lead to an increase in the frequency.

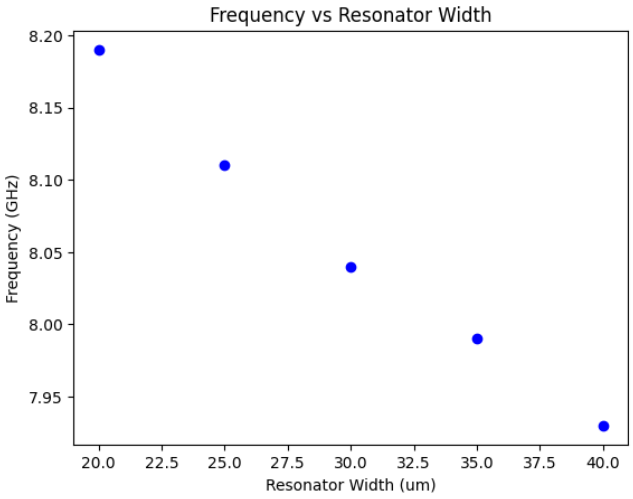

Figure 20: Relation of frequency with the resonator width

Furthermore, in Figure 20, changes to the width of the resonator demonstrated an inverse relationship with frequency. As the width of the resonator increased, there was a notable decrease in the resonant frequency. This effect can be attributed to increased capacitance, which tends to lower the resonant frequency, which can be easily obtained from the basic resonator frequency equation that is mentioned in the theory section. We initially chose a 30 um resonator gap and a 30 um resonator width based on the graph.

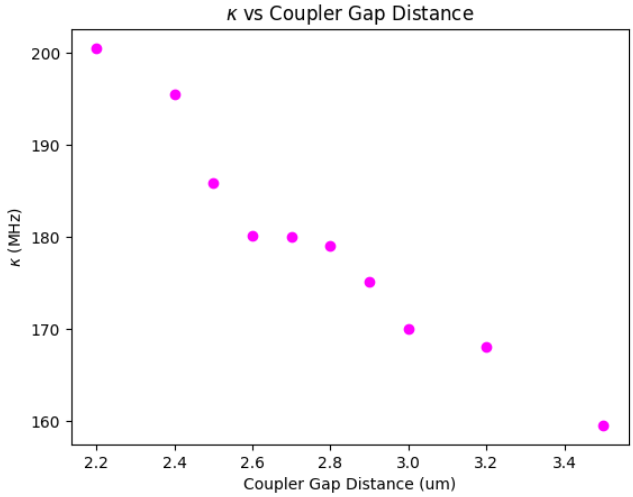

Figure 21: Relation of κ with the coupler gap distance

After exploring the amplifier's frequency, attention was shifted towards examining κ values directly influenced by the coupler gap distance. As detailed in Figure 21, a discernible decrease in kappa correlates with an increase in the coupler gap distance. The graph is representative of the anticipated outcome, as it has a direct impact on the coupling capacitance value and consequently influences the coupling strength. The resonator's length is another parameter significantly affecting the κ value, as in Figure 22. For an increase of almost twice as much, the kappa value decreases by almost half. The impact of length on frequency and kappa, displayed in Figure 15 and Figure 22, is substantial. Therefore, I changed the length slightly during the design process.

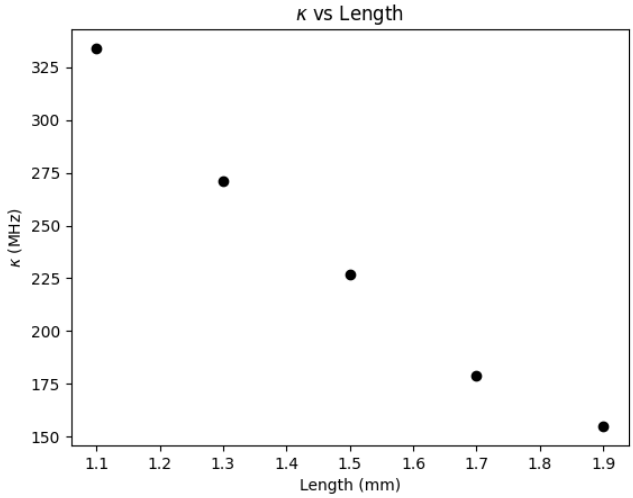

Figure 22: Relation of κ with the resonator length

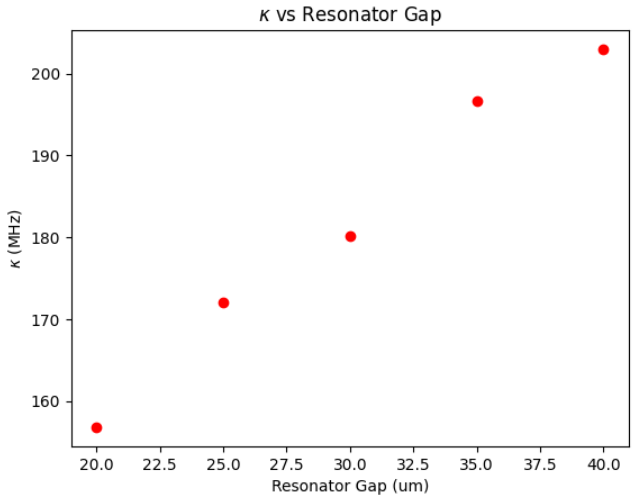

Figure 23: Relation of κ with the resonator gap distance

Additionally, analysis of the resonator gap distance in Figure 23 revealed that the kappa value increases as the gap is widened. Specifically, when adjusting the resonator gap from 20 µm to 40 µm, the kappa values were observed to range from approximately 95 MHz to 205 MHz. The increase in performance is due to the improved coupling efficiency and lower damping effects that come with a larger gap, which results in lower resonator capacitance. The wider gap appears to enhance the interaction between the resonator fields and the connected transmission line, leading to an increase in the κ value.

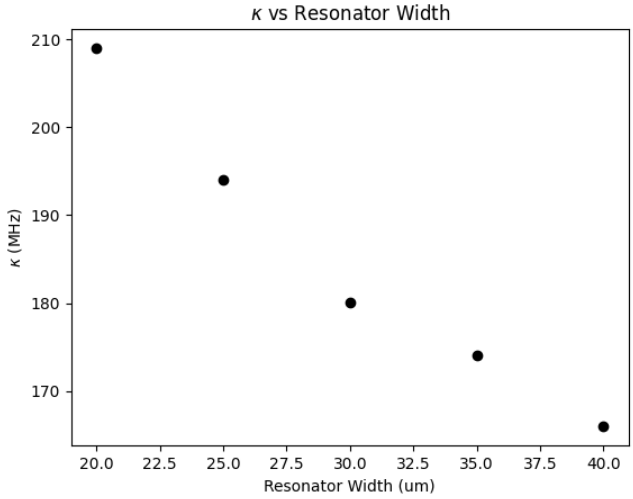

Figure 24: Relation of κ with the resonator width

Finally, our investigation extended to understanding how changes in the resonator width impact the kappa values. Keeping the range consistent with that of the resonator gap, it was noted that increasing the width of the resonator led to a decrease in kappa values from 210 MHz to 170 MHz. The opposite situation can be considered for the resonator gap. Hence, the coupling strength decreases with increasing resonator capacitance value.

In the ongoing parameter analysis for Step 2 of the design methodology, we focus on the amplifier capacitance and the Kerr value. To achieve this, we are utilizing the COMSOL Multiphysics simulation program.

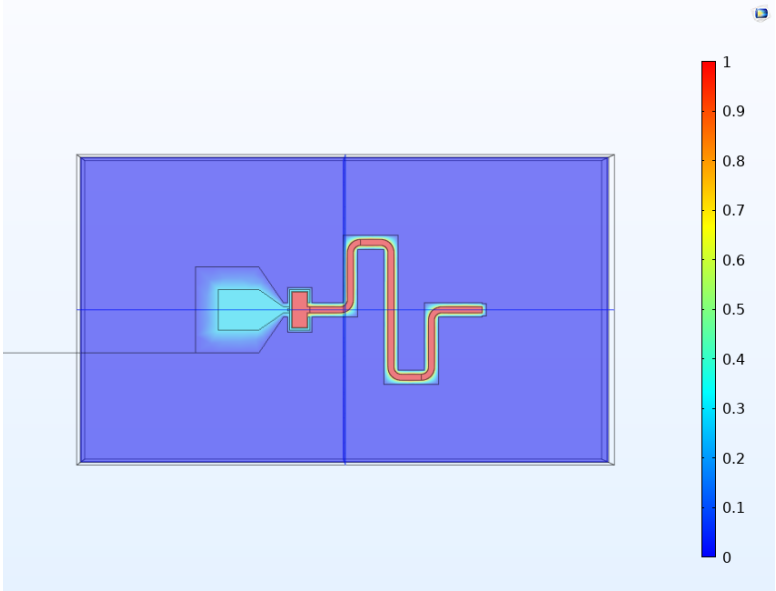

Figure 25: Electric potential in the amplifier in COMSOL

The electric potential distribution image from COMSOL provides crucial insights into the functionality and performance of your Josephson Parametric Amplifier design. High potential regions (red) indicate areas with strong electric fields, which are effectively confined within the resonator. The intermediate potential regions (yellow) inside the gaps are essential for coupling and energy transfer, facilitating interactions within the resonator. The launchpad's low potential regions (blue) represent areas of low

electric potential. Since the gap between the launchpad and the ground is higher than that of the resonator, the resulting capacitance value will be lower, so this potential is expected.

	Launchpad	Resonator
Launchpad	1.750E-13 F	-5.302E-14 F
Resonator	-5.302E-14 F	3.191E-13 F

Table 1: Maxwell Capacitance Matrix

The crucial outcome of the COMSOL simulation is the Maxwell capacitance matrix, which is a mathematical representation used in electromagnetics to describe the capacitive interactions between a set of conductors in a system. The diagonal elements of the matrix represent the self-capacitance of the conductors, while other elements represent the mutual capacitance between conductors. In this circuit, there are two conductors, one of which is the launchpad, and the other one is a CPW resonator. In Table 1, the first element(C_{11}) represents the capacitance of the launchpad to the ground, and the second element(C_{22} is for the resonator capacitance to the ground. The off-diagonal elements represent the coupling capacitance value between these components, which has a negative sign. According to the definition of capacitance C, where $C = \frac{dQ}{dV}$ a negative capacitance implies that an increase in voltage (V) would lead to a decrease in the stored charge (Q). This phenomenon can theoretically occur when an increase in potential causes a reduction in the population of interfacial states [28].

In this part of the design process, we decided on the capacitance value of the resonator together with the COMSOL simulation and calculated the Kerr coefficient by putting this inductance value into the Equation 27 since we cannot obtain this value in any simulation program.

In Figure 26, the graph indicates a clear relationship between coupler gap distance and capacitance values, showing that capacitance decreases with notable variations at specific points as the gap increases.

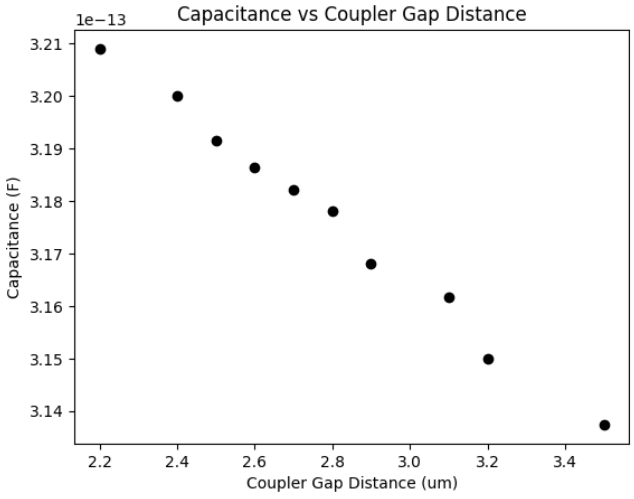

Figure 26: Relation of the resonator capacitance with the coupler gap distance

Figure 27 shows other relations between the capacitance of the resonator and the resonator gap. This can be easily explained by considering the simple capacitance formula: as the resonator gap increases, the distance between the two plates of the capacitor increases, leading to a decrease in capacitance value.

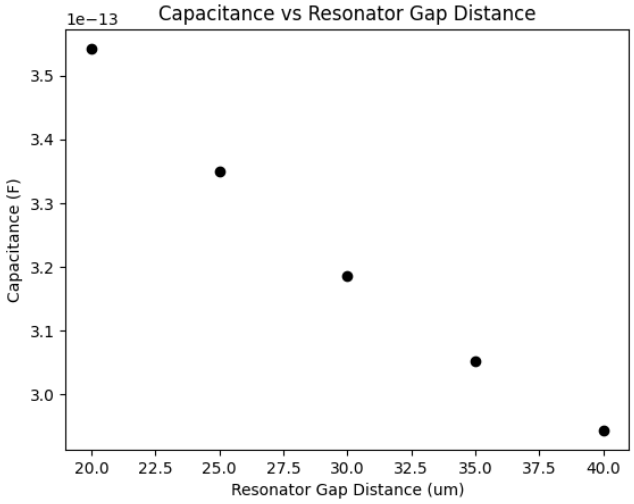

Figure 27: Relation of the resonator capacitance with the resonator gap distance

Similarly, the opposite situation can be seen in Figure 28 for the resonator width. The capacitance increases steadily as the resonator width ranges from 20.0 µm to 40.0 µm, indicating that a wider resonator enhances the resonator's capacitance.

Understanding these relationships in the graphs is crucial for designing resonators with specific capacitance characteristics. This insight helps optimize resonator dimensions for the parametric amplifier, as the resonator's capacitance values directly affect the Kerr coefficient.

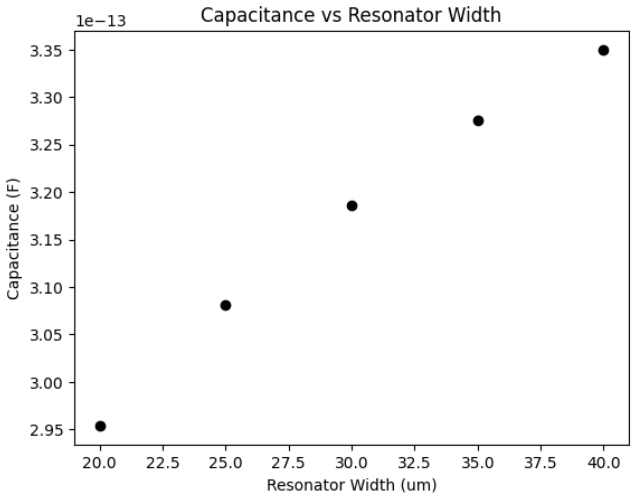

Figure 28: Relation of the resonator capacitance with the resonator width

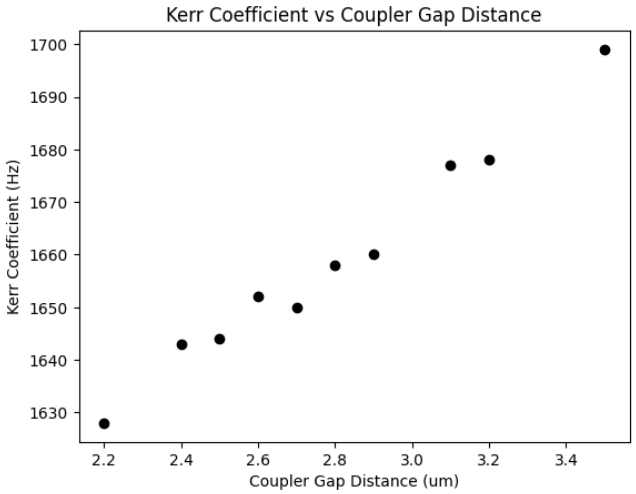

Figure 29: Relation of the Kerr coefficient with the coupler gap distance

In the following analysis, we will investigate the correlation between the coupler gap distance and Kerr values. Figure 29 presents the relationship between the coupler gap distance and the Kerr coefficient for a Josephson parametric amplifier. The data indicate that as the coupler gap distance increases from 2.2 µm to 3.0 µm, the Kerr coefficient generally exhibits an upward trend.

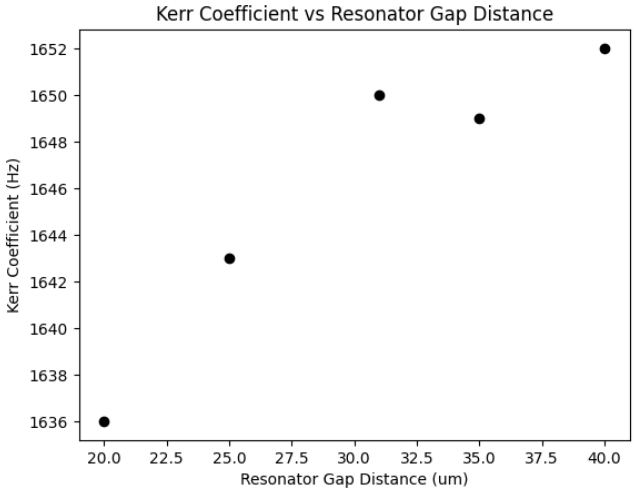

Figure 30: Relation of the Kerr coefficient with the resonator gap distance

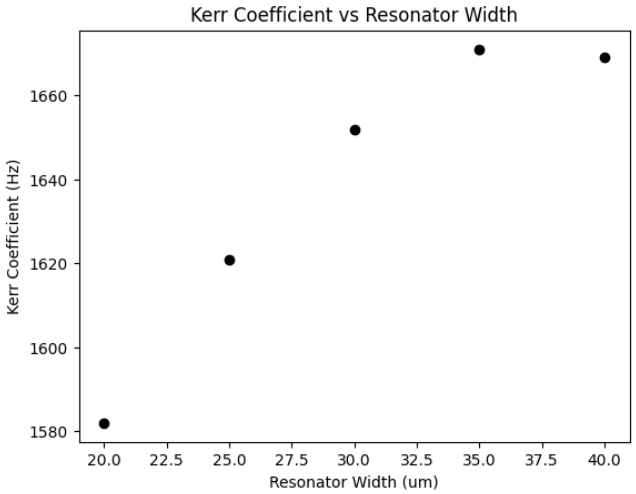

Figure 31: Relation of the Kerr coefficient with the resonator width

Both graphs (Figures 30 and 31) show a consistent trend of increasing Kerr coefficient with both increasing resonator width and gap distance, albeit slight variations at specific points. The observed pattern suggests that these geometric parameters significantly impact the nonlinearity in Josephson parametric amplifiers. Adjusting the resonator width and gap distance alters the effective inductance and capacitive coupling within the resonator, thereby affecting the system's Kerr nonlinearity as in Equation 27. Since this equation contains many parameters and nonlinear functions, these graphs allow us to predict the behaviour of Kerr values more clearly.

Our design process begins by selecting initial parameters. The starting point chosen includes a resonator length of 1.7 mm, a resonator width of 30 µm, a resonator gap of 30 µm, and a coupler gap distance of 2 µm. In the first step of the design process, Initial parameters produced a frequency of 7.93 GHz and a kappa value of 203 MHz. Based on the graphs obtained from simulations to investigate parameter behavior, we initially obtained lower κ values, with the lowest around 117 MHz at 8.04 GHz, by adjusting the length to 1.47 mm, the resonator width and gap distance to 45 µm and 15 µm respectively, and the coupler gap to 4 µm. However, using these parameters resulted in a Kerr coefficient that was more than twice our target value, around 2000 Hz.

To address this, we adjusted the length of our parametric amplifier to 1.68 mm to enable operation at 8 GHz. Additionally, by reducing the resonator width and gap to 15 µm and the coupler gap to 2.5 µm, the linewidth (κ) was set to 168 MHz. While this κ value is relatively high, it was chosen after careful consideration of the Kerr coefficient, which was reduced to 1645 Hz. The Kerr value could not be obtained lower than this value, and very high kappa values were encountered when attempted. This compromise ensured optimal performance and stability of the amplifier.

In designing the second amplifier for operation at 7 GHz, we utilized a methodology similar to the one used for the first amplifier. Initially, we set the resonator width and gap distance to 20 µm, the length to 2 mm, and the coupler gap distance to 2 µm. These initial settings resulted in a frequency of 7.19 GHz and a kappa value of 154 MHz, which were significantly off our target values. We first adjusted the length, increasing it to bring the frequency closer to 7 GHz. Next, we focused on optimizing the kappa value by incrementally increasing the resonator width up to 30 µm. This adjustment caused the frequency to deviate, which we then corrected by fine-tuning the coupler gap distance and length.

In our final design, we achieved the desired specifications with a width of 30 µm, a length of 2.05 mm, and a coupler gap distance of 2.6 µm while maintaining the initial resonator gap distance. This optimized configuration resulted in a frequency of 7.002 GHz, a κ value of 112 MHz, and a Kerr coefficient of 1239 Hz. By reducing the resonator gap to 30 um and the coupler gap distance to 2.6,

the Kerr value was slightly lowered to 1105 Hz. But this final value resulted in a 4 MHz increase in the kappa value.

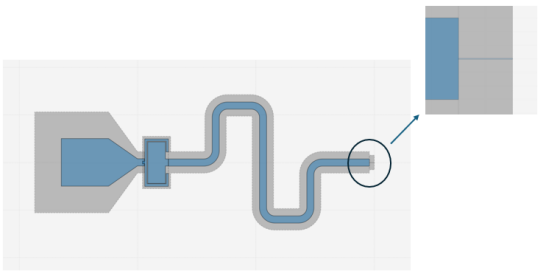

(a) JPA in Qiskit Metal

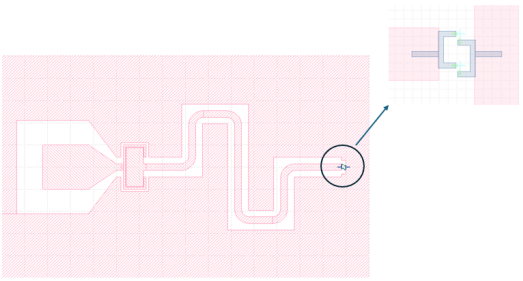

(b) JPA in KLayout

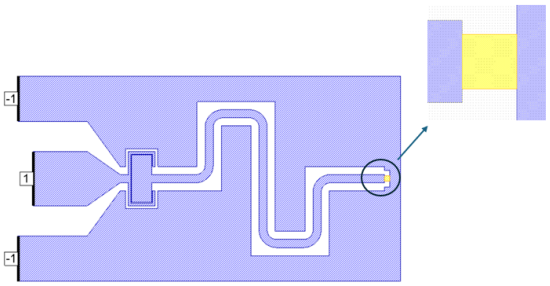

(c) JPA in Microwave Office

Figure 32: The parametric amplifier in different software

Displayed in Figure 32 is the design and simulation of the Josephson parametric amplifier, operating at approximately 8 GHz, conducted using multiple tools: Qiskit Metal, KLayout, and Microwave Office.

In Figure 32 (a), Qiskit Metal uses a placeholder or "fake junction" to represent the SQUID in the amplifier design. This placeholder is designed to match the length of the actual SQUID and approximate the physical layout accurately. However, due to current limitations in Qiskit Metal's ability to model SQUIDs directly, this placeholder does not capture all the intricate details of the SQUID's behavior.

The detailed layout of the amplifier in Figure 32 (b), including the SQUID, was created using The KLayout tool. The image from KLayout displays the design with the actual SQUID implemented. The difference in etching space at the end of the resonator observed in the layout, larger than that of the Qiskit Metal design, is due to the precise modeling of the SQUID in KLayout. The variance

is approximately 30 micrometers, allowing us to position the SQUID between the resonator and the ground easily. This is crucial because the KLayout file will be used in the fabrication stage of the chip.

In Figure 32 (c), the circuit in the Microwave Office circuit displayed an amplifier concludes with a simulated junction featuring a kinetic inductance set at 1 nH, emulating the SQUID inductance of 1 nH. In our practical circuit, the junction inductance supersedes kinetic inductance. The utilization of kinetic inductance in this context stems from its adjustable nature; altering the inductance value merely entails drawing a basic square shape within the simulation platform. While the blue structures depicted in the illustration may encompass materials with significant kinetic inductance, such as NbTiN (niobium titanium nitride), they are treated strictly as conductive elements, with their kinetic inductance factored at zero, even when in the real world it has a small amount of kinetic inductance.

2.4 Final Chip Design

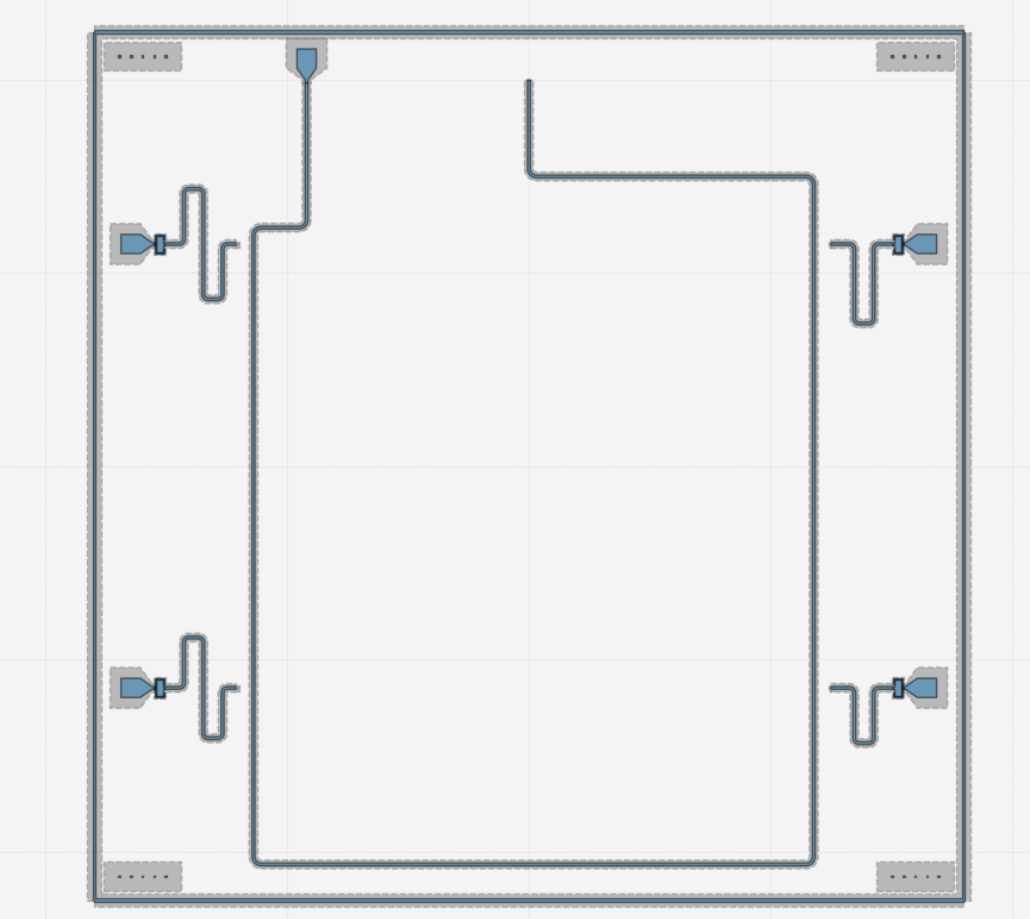

Figure 33: Final design of the chip

Using a similar method, we designed the chip with four JPAs operating in different frequency ranges. The use of four different amplifiers allows us to easily amplify the signal at different readout frequencies by choosing the suitable amplifier.

The first amplifier, located at the top left of Figure 33, features a 30 µm resonator gap, 40 µm resonator width, 2.9 mm length, and 2.5 µm coupler gap and operates at 6 GHz. This amplifier has a κ value of 82 MHz and a Kerr coefficient of 695 Hz. The second amplifier, located at the bottom left of the figure, operates at 6.4 GHz with a 30 µm resonator gap, 30 µm resonator width, 2.55 mm length, and

a 2.3 µm coupler gap. It has a κ value of 93 MHz and a Kerr coefficient of 860 Hz. The third and fourth amplifiers, mentioned in the previous section, operate at 7 GHz and 8 GHz and are located in the figure's upper right and lower right corners, respectively.

Through precise parameter selection and adjustment, including resonator gap, width, length, and coupler gap, we have effectively optimized performance across various frequency ranges. This meticulous design process has resulted in enhanced kappa values and Kerr coefficients.

In the middle of the figure, a flux line was positioned to allow adjustment of the magnetic flux of the SQUIDs in the JPAs. Although the inductance is set at 1 nH with this magnetic flux, there may be cases where we need to change the inductance. For instance, if a 6 GHz amplifier is employed for the readout frequency at 5 GHz, adjusting the magnetic flux allows for tuning to the proper frequency.

Positioning the flux line close to the amplifiers in the chip design was a deliberate choice to optimize the performance of the high-frequency parametric amplifiers. This proximity ensures that magnetic flux couples to the SQUIDs within the amplifiers, allowing for fine-tuning of the operating point. Additionally, the design minimizes flux leakage to other parts of the chip, reducing the risk of unintentional coupling and interference with other components.

On the other hand, the resonance frequencies of these amplifiers can be determined by observing the phase changes in the parameter S_{11}. Figure 34 clearly demonstrates the phase change graph for the reflection coefficient of the amplifier. Each plot shows a distinct peak at its respective frequency, highlighting the precise tuning of these amplifiers to their target frequencies. The red graph corresponds to the amplifier designed for 6 GHz and exhibits a sharp dip at this frequency, indicating a strong resonance. Adjacent in green is the graph for the 6.4 GHz amplifier, which shows a similar yet slightly shifted resonance behavior. The other graphs, in purple and blue, represent the resonance frequencies of the amplifiers at 7 GHz and 8 GHz, respectively. It indicates that the frequencies are set as determined.

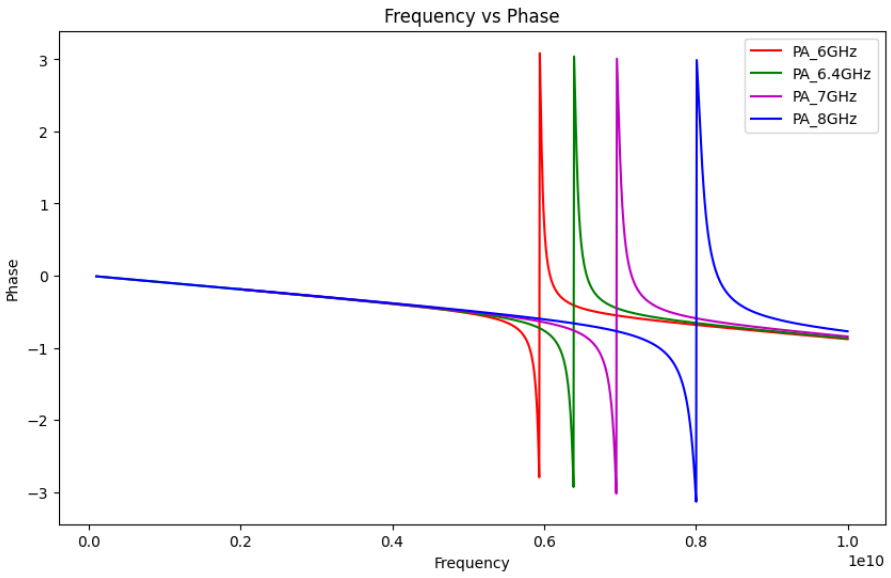

Figure 34: Changes in the phase of reflection coefficient(S_{11}) for different designed JPAs

3 Design of Amplifier Enclosure

The chip is mounted in a sample package that is thermally connected to a dilution refrigerator's coldest stage. This setup defines the immediate electromagnetic environment of the amplifiers, necessitating a structure that protects the chip from unwanted effects. In this section, we will present the design of the enclosure, whose primary goal is to shield the Josephson parametric amplifier from environmental interference while ensuring its efficient control and thermal management. With its carefully engineered design, the package can serve as a 3D cavity with an engineered mode spectrum, providing an electromagnetic environment that suppresses spurious modes within the frequency spectrum of interest [29]. However, the package prevents external losses; it can induce other loss channels, which can be considered in our design, such as box modes.

3.1 Parameter Target

In enclosure design, two factors need to be considered. The first is thermalization, which refers to achieving thermal equilibrium within the enclosure containing the chip and its components. Using a metal with minimized thermal conductive loss is preferable, increasing thermal conductivity and effective thermalization, leading to the chip reaching and remaining close to the base temperature. Among typical metals, such as aluminum and copper, aluminum is generally favored due to its low cost and lightness, which can not make a difference in small-scale enclosures. However, aluminum's high electrical conductivity makes copper the better choice due to its superior thermal and electrical conductivity. Around 20mK near the base temperature in the refrigerator, copper's thermal conductivity is 20 times larger than aluminum's, which is crucial for efficient thermalization and electromagnetic shielding. Besides, conductive adhesives with high thermal links, a hundred times larger than copper's thermal conductivity, could be preferred. This efficient heat transfer reduces thermal resistance and improves overall cooling performance. However, their low conductivity would have increased conductivity losses; therefore, they were not used [30].

The second part is the box or cavity modes. The enclosing metal rectangular cavity, which is typically employed to minimize radiative losses from the chip and substantially reduce the number of environmental modes, generates these modes. They are standing waves of the usual TE and TM waveguide modes [31] and interact directly with the chip. The frequencies of the transverse electric (TE_{nml}) and transverse magnetic (TM_{nml}) modes in a rectangular cavity are expressed as follows:

$$f_{nml} = \frac{c}{2\pi\sqrt{\mu_r \epsilon_r}} \sqrt{\left(\frac{n\pi}{a}\right)^2 + \left(\frac{m\pi}{b}\right)^2 + \left(\frac{l\pi}{d}\right)^2} \tag{31}$$

In the 31, μ_r is the relative permeability, ϵ_r is the relative permittivity, c is the speed of light, and a, b, d are the three dimensions of the cavity. The components μ_r, ϵ_r, and c depend on the medium carrying the mode, typically the dielectric. Adjusting the dimensions can exclude box modes from the desired frequency domain. The cavity walls should also be positioned away from the chip to reduce material-induced dissipation. All the things should be handled during the design process [30].

3.2 Computer Aided Design(CAD)

The microwave properties of the package are analyzed using the 3D finite element simulation software COMSOL Multiphysics. The simulation involves creating a detailed model of the enclosure design, including all relevant geometric features and material properties. Electromagnetic simulations are then performed to evaluate the behavior of the transverse electric (TE) and transverse magnetic (TM)

modes within the cavity. This analysis helps in understanding the impact of the enclosure design on the performance and efficiency of the microwave components, ensuring optimal design parameters are achieved for minimizing losses and suppressing the package modes.

3.3 Final Enclosure Design

In the initial design, the base and lid parts of the rectangular enclosure are created. As a material, we used Oxygen-Free Electronic Copper, which has a purity of 99.99 percent copper and an oxygen content of 0.0005 percent. This type of copper offers higher electrical and thermal conductivity than standard copper, making it ideal for applications where efficient energy transfer is crucial, such as preventing overheating on the chip.

In Figure 35, it can be seen the base part of the enclosure. The small raise, whose height is adjusted by that of the PCB, in the middle part lets the chip be put on it; moreover, on each side, there are slots for the SMA's head and the two forked spaces for the SMA connectors' prongs, which helps connect the PCB with the feedline. At every corner, it can be seen the screw holes for each of them gather different parts of the structure. One is for making the PCB stable, the other is for setting the enclosure on the bracket, and the third is for sticking the lid to the base part.

Figure 36 shows the upper part of it, called the lid. Most parts at the top of the lid, such as slots for SMA's and screw holes, complement each other with the parts at the bottom; the important part is the space above the chip and the transmission lines, which creates boxlike cavities. Many factors were considered when calculating these sections' lengths, widths, and heights. The first was that not much distance was desired between these gaps around the transmission line on the PCB; at the same time, gaps were left around the chip as much as the wire bonds could be placed. Apart from this, these height settings were made. The space at the top of the chip is around $7\,\text{mm} \times 7\,\text{mm} \times 1.45\,\text{mm}$, and it connects the cavity above the transmission line on the PCB, which has dimensions $1.2\,\text{mm} \times 10.45\,\text{mm} \times 1.45\,\text{mm}$.

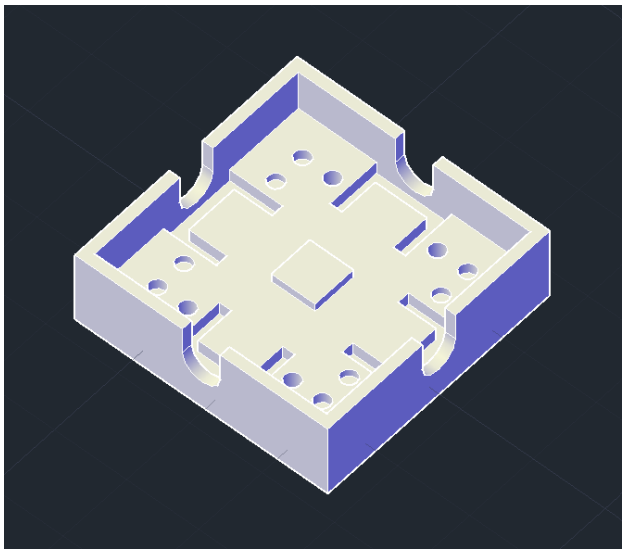

(a) Perspective view

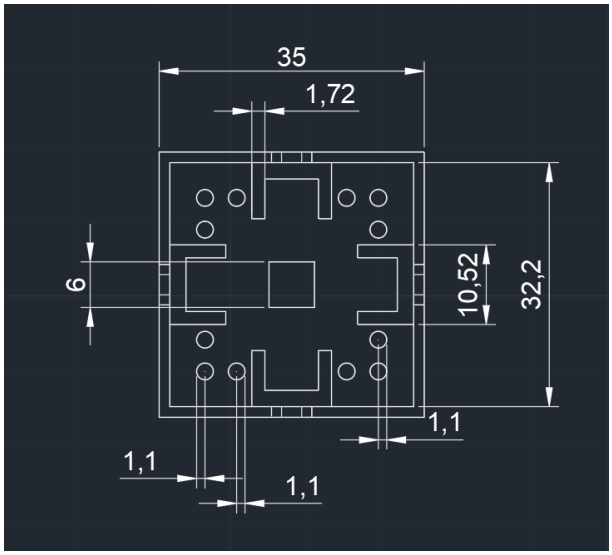

(b) Top view

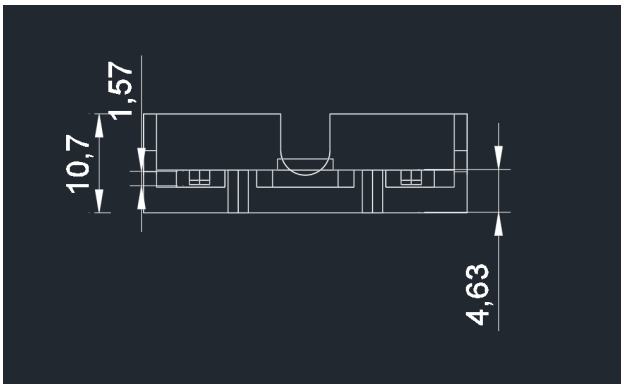

(c) Front view

Figure 35: Bottom Part of the Enclosure

For the starting point of the design, the box mode equation was utilized. Since the largest cavity is on the chip, which mostly creates the resonant cavities ruining the run of the amplifier, the others were neglected, and a very rough analysis of the mode that can be in a cavity was performed. In the table 2, the TE frequencies are shown for the $7\,\text{mm} \times 7\,\text{mm} \times 1.25\,\text{mm}$ cavity. Since the TE_{mnl} and TM_{mnl} modes, mnl, all nonzero, are always degenerate, only the TE modes can be represented. From this table it can be deduced that the undesired modes inside the enclosure are far beyond our operating frequency range. We use the Comsol simulation to verify this obtained information

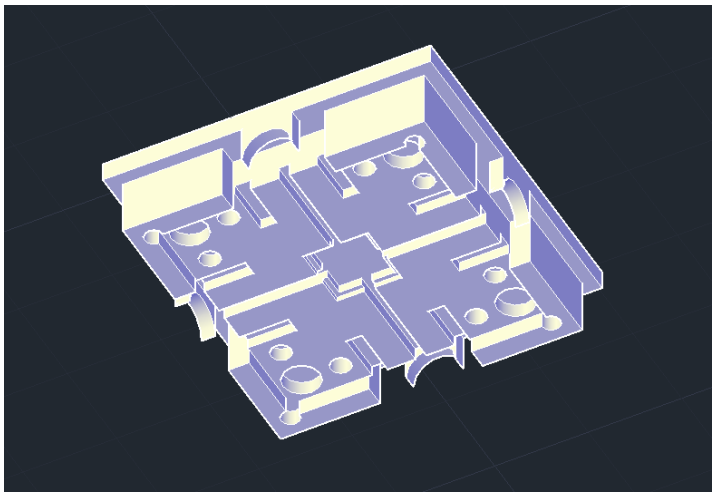

(a) Perspective view

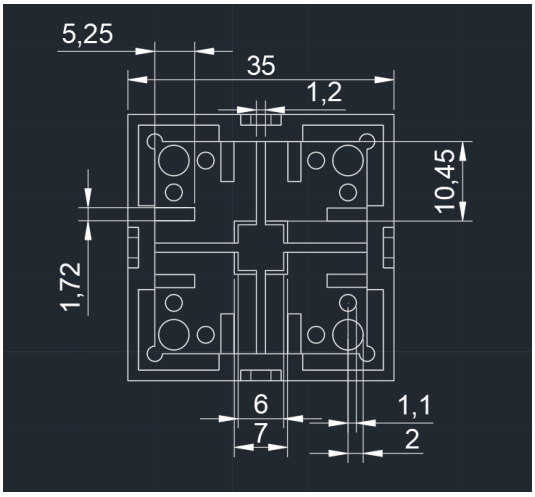

(b) Top view

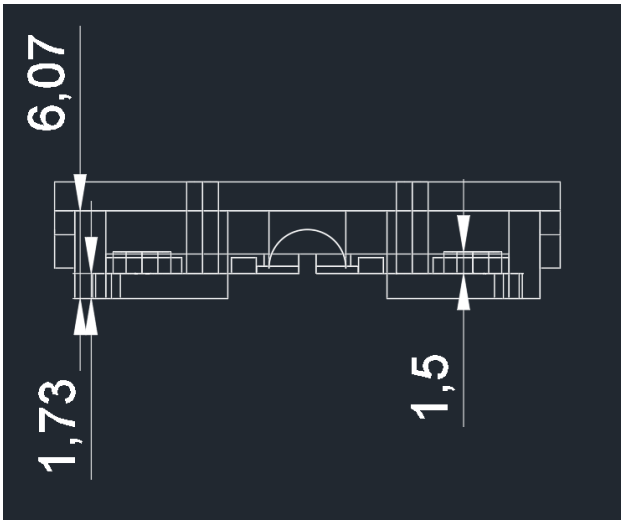

(c) Front view

Figure 36: Lid of the Enclosure

Mode (n, m, l)	TE(TM) Mode Frequency (GHz)
$(0, 1, 0)$	21.42
$(1, 0, 0)$	21.43
$(1, 1, 0)$	30.30
$(0, 2, 0)$	42.85
$(2, 0, 0)$	42.85
$(1, 2, 0)$	47.91
$(2, 1, 0)$	47.91
$(2, 2, 0)$	60.60

Table 2: Calculated TE and TM mode frequencies for a rectangular cavity with dimensions 7 mm × 7 mm × 1.45 mm.

We use the simulation to validate the obtained information. COMSOL simulation specifically focused on the standing wave patterns within the cavity. In Figure 37, the enclosure has been simplified by removing the screw holes and the SMA connector components, allowing for simulation and observation of the box modes within the enclosure. As a material, oxygen-free copper is used, and the relative

permittivity (ϵ_r) and relative permeability (μ_r) of copper are often approximated as 1 because copper's high conductivity predominantly determines its response to electromagnetic fields, making the effects of its intrinsic permittivity and permeability negligible. The initial configuration involved a cavity with a height of 1.45 mm above the chip.

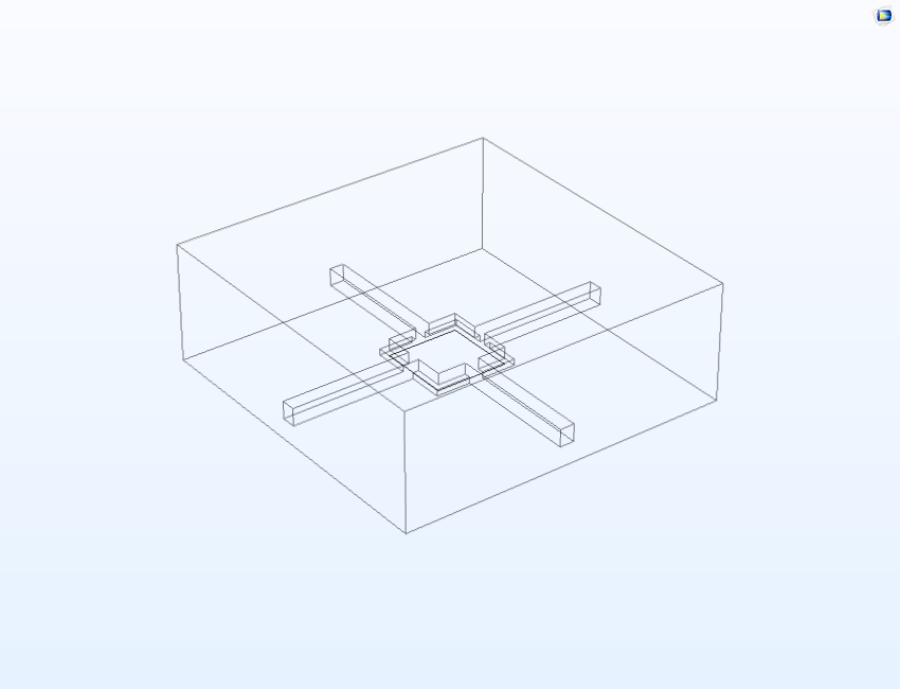

Figure 37: The simplified setup version of the enclosure

We performed the first simulations by inserting the silicon chip. The simulation results, as shown in Figure 38, indicate the presence of a standing wave at the center of the cavity with an eigenfrequency of 8.0095 GHz, which lies within the amplifier's operational frequency range and can interfere with the amplifier's performance. It can be stated that This is different and unexpected from the results in the table 2. The reason for this is obvious, because the enclosure in the simulation program departs from a simple rectangular waveguide by its complex structure, incorporating intricate cavities. Also, the silicon chip with high dielectric constant is used. The distribution of the electromagnetic field and, consequently, the resonant frequencies can be dramatically changed by these extra features, and it may drop from 21GHz to around 8GHz.

Although the Equation 31 does not precisely match the designed cavity, it indicates that reducing the dimensions will result in an increase in frequency. This implies that it is needed to decrease the design heights, particularly the height of the cavity above the chip, which has the largest volume. In the simulation, the heights of the cavity are gradually reduced. Simulations with reduced heights of 1.35 mm and 1.25 mm resulted in only minor frequency shifts around 10 MHz in the order of MHz, suggesting limited effectiveness.

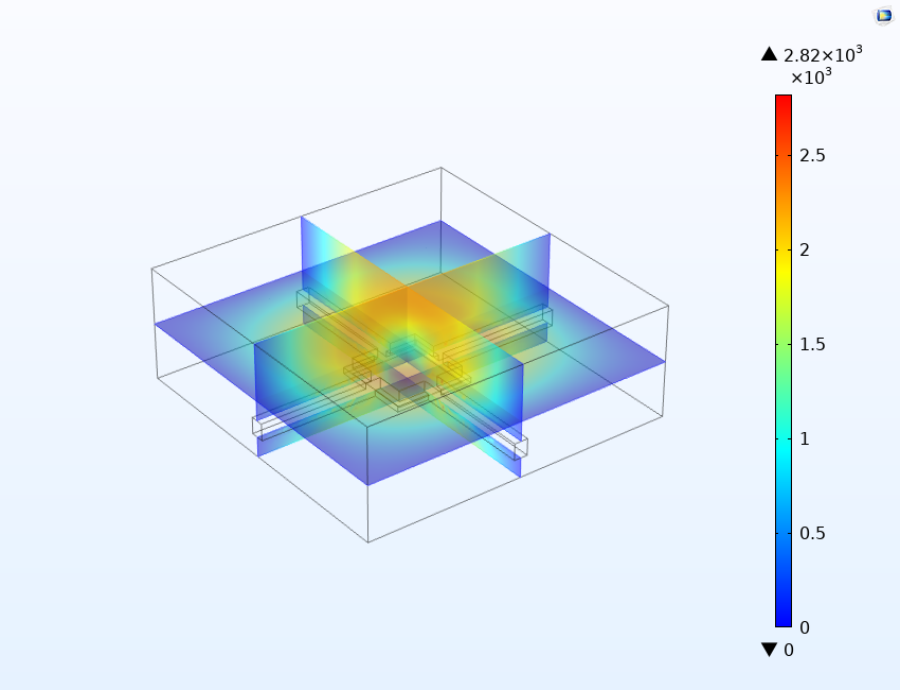

Figure 38: Electric field distribution inside the enclosure with a cavity height of 1.45 mm

The minimal shift is likely due to the absence of the printed circuit board (PCB) with FR4, an epoxy resin composite, which would provide a more accurate representation of the system [32]. Given that the relative permittivity of FR4 is 4.5, we can anticipate a frequency decrease of approximately 2 times or more. While this decrease may shift the box mode close to, or possibly beyond, the acceptable frequency limit, the effect of the modes can still be observed within the range. This is due to the Lorentzian distribution of these modes, which may influence signals in the 4-8 GHz range.

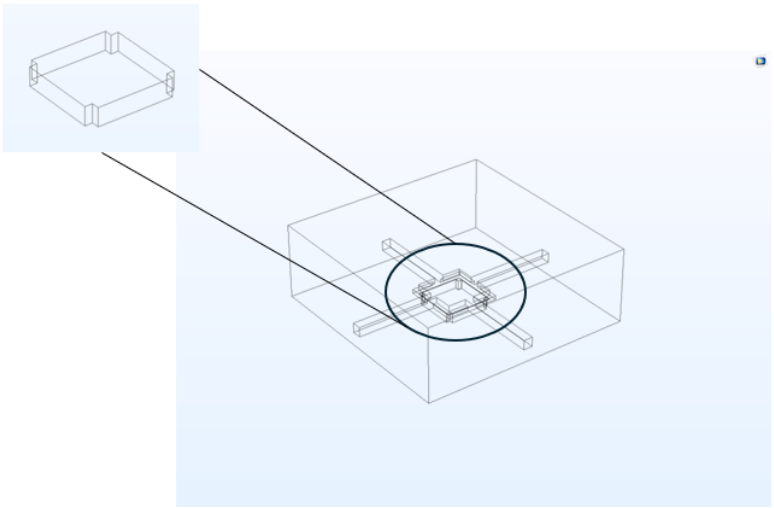

Figure 39: Simplified version of the new design with drilled out the chip and the part that is drilled as zoomed in

In accordance with Lienhard's paper [29], a novel design approach was implemented. The bottom of the chip was hollowed out, and the chip was placed on top of four columns. Figure 39 shows a simplified version of the enclosure with drilled part. Here, the height of the top was kept constant at 1.25, and the height of the cavity was changed from 1.2097 mm to 1.4097 mm. In Figure 40 (a), it can be observed that this cavity lowers the frequency. At a height of 1.2097, a spurious mode was obtained at 7.59 GHz. However, as can be seen from the figure, at the height of 1.4097 mm in Figure 40 (b), there was no change in frequency, but there was a large improvement in the magnitude of the electric field inside the cavity, especially around the chip, from 5 V/m to 4 V/m.

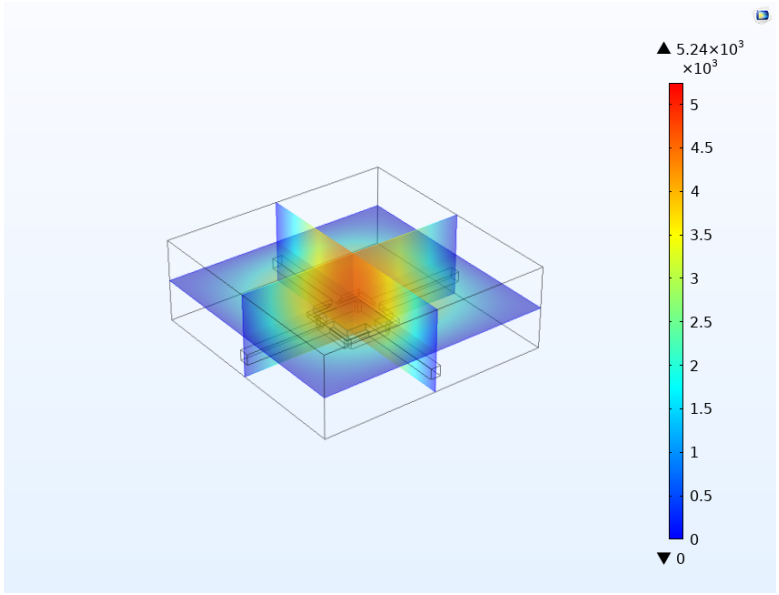

(a)

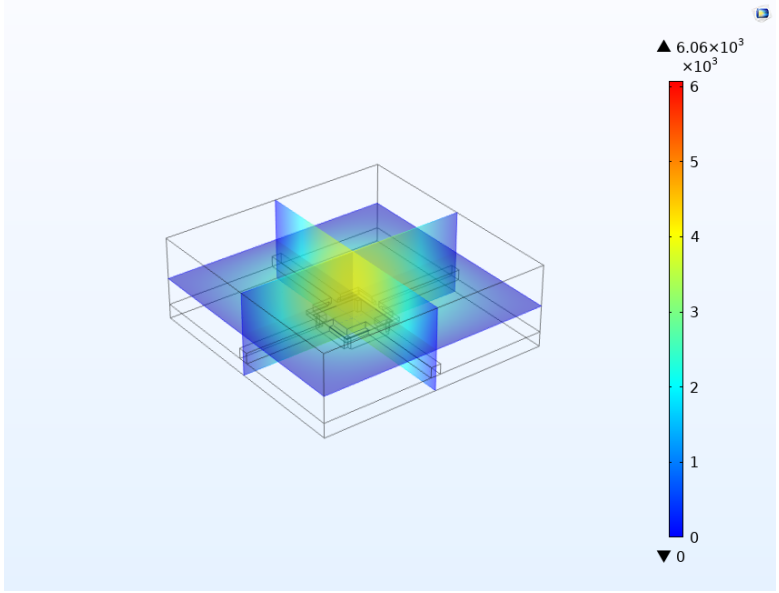

(b)

Figure 40: (a)Electric field distribution of 1.2097 mm drilled design (b) Electric field distribution of 1.4097 mm drilled design

3.3.1 Alternative Enclosure Design

After getting undesired results with box modes in the amplifier's operational region, we used the alternative enclosure called "Octobox." due to its geometric design featuring elements based on the number eight. Figure 41 (a) and (b) show the lid and the base of the enclosure. Part (c) depicts the PCB design that is suitable for this enclosure. The fact that it is made of copper is also an advantage in terms of thermalization and electrical conductivity, as mentioned in the previous section.

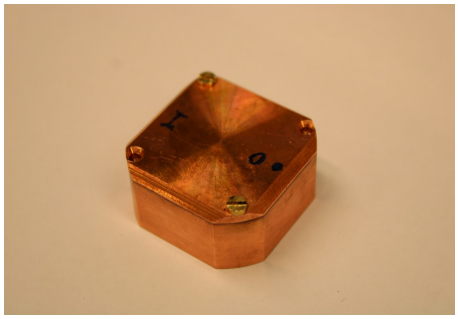

(a) General view of the octobox

(b) Base part of the octobox

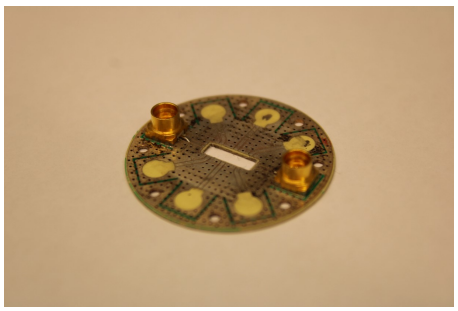

(c) PCB of the octobox

Figure 41: Octobox

The enclosure is being analyzed to determine its suitability for avoiding spurious modes within the desired frequency range. The S_{12} parameters of the octobox were measured with lids made of materials with different thermal conductivity. In Figure 42, the red line represents the signal when no element corresponds to the noise. The orange and blue lines indicate the performance of the PCB with a copper lid and the PCB with an aluminum lid, respectively. Between 4GHz and 8.5GHz, there seems to be no significant difference. However, after 8.5GHz, conductor loss occurs due to the high conductivity of copper. This can be attributed to the skin effect or surface roughness. Copper's higher electrical conductivity compared to aluminum results in a smaller skin depth at high frequencies, increasing the effective surface resistance of copper and leading to higher losses and lower transmission efficiency. Additionally, if the copper lid has a rougher surface compared to the aluminum plate, it can lead to increased scattering of electromagnetic waves, resulting in higher losses and lower S_{12} parameters [33]. The purple line represents the inclusion of all elements with a copper lid. It can be observed that there are box modes between 4-8GHz.

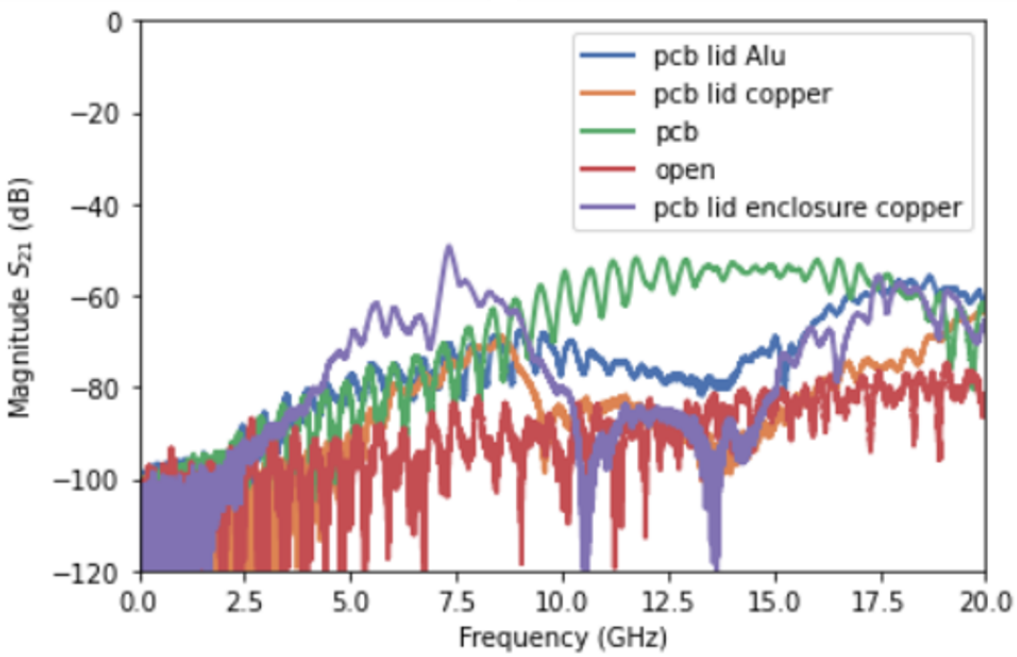

Figure 42: S_{11} parameters of the octobox with different components

Conclusion

In this study, the goal was to develop four Josephson Parametric Amplifiers (JPAs) specifically for fluxonium qubit readout signal, with a target operational frequency range of 4-8 GHz and was to enhance the dynamic range of these amplifiers to achieve improved performance for the fluxonium readout. Additionally, a suitable enclosure had to be designed to ensure the JPA's practical application.

The JPA was optimized according to specific target parameters to enhance their performance. The primary parameter, the κ value of 100 MHz, was chosen to define the desired bandwidth and thereby determine the quality factor of each amplifier. The second key parameter, the Kerr coefficient, was targeted at 1000 Hz to assess the nonlinearity of the amplifiers. By optimizing these parameters, we aimed to expand the dynamic range of the JPAs, which typically exhibit low dynamic ranges, and to design circuits capable of handling high-amplitude signals by increasing the saturation power.

Throughout the design process of the JPA, a systematic methodology has been employed, making use of the advanced simulation tools Qiskit Metal, Microwave Office, and Comsol. This approach allowed us to fine-tune critical design aspects such as resonator gap, width, length, and coupler gap. These adjustments were crucial in achieving the specific κ values and Kerr coefficients for each design. Consequently, four amplifiers with distinct specifications were developed: the first operates at 6 GHz with a Kerr value of 695 Hz and a κ value of 82 MHz; the second at 6.4 GHz with a κ value of 93 MHz and a Kerr value of 859 Hz; the third at 7 GHz with a κ value of 116 MHz and a Kerr value of 1105 Hz; and the final amplifier at 8 GHz with a κ value of 168 MHz and a Kerr value of 1645 Hz.

Optimizing the κ and the Kerr values simultaneously has posed itself to be a significant challenge in the optimization process, resulting, at times, in considerable deviations from the targeted values. While it was possible to align the kappa values with our goals closely, the Kerr values significantly diverged. To tackle this issue, multiple objective optimization (MOO) was turned to in order to refine the approach and better align with the desired parameters. Regrettably, the distributed element model did not yield successful outcomes in this particular scenario, leading to a reversion to the original methodology. Despite these challenges, given the circumstances, every effort was made to achieve the most optimal results possible.

For the enclosure design, simulations aimed at optimizing the cavity modes to lie outside the critical 4-8 GHz frequency range. Despite these efforts, the initial enclosure design with a cavity height finalized at 1.25 mm resulted in a mode around 8 GHz, unfortunately falling within the target range. This persistent mode could not be eliminated, leading to exploring an alternative enclosure design. However, similar challenges were encountered with the new enclosure, as its box modes also resided within the operational frequency range.

In further study, various techniques for parametric amplifiers can be taken into consideration. One of them is to use broadband techniques for parametric amplifiers to enhance the bandwidth and saturation power of the JPA by a structure such as a transmission line impedance transformer. The structure can help reduce the input line impedance, leading to a subsequent decrease in the resonance Q factor without increasing the chip space [34]. In addition to this, by increasing the number of SQUIDs in the arrays, using Josephson junctions with even larger Josephson energy, and increasing κ, it should be easy to achieve further improvements in the dynamic range [35].

For the enclosure design, the different cavity shapes above the chip part can be considered, such as a dome or spherical cavity. A spherical cavity has the potential to enhance the design and performance of microwave packages significantly. It can be leveraged to shift resonant frequencies effectively. Also, It exhibits fewer higher-order modes within a given frequency range, thereby reducing mode density and simplifying the mode structure. This can lead to improved performance and reduced interference from unwanted modes [36, 37].

References

[1] Taryn V Stefanski and Christian Kraglund Andersen. Flux-pulse-assisted readout of a fluxonium qubit. *arXiv preprint arXiv:2309.17286*, 2023.

[2] Lukas Johannes Splitthoff, Jaap Joachim Wesdorp, Marta Pita-Vidal, Arno Bargerbos, and Christian Kraglund Andersen. Gate-tunable kinetic inductance parametric amplifier. *arXiv preprint arXiv:2308.06989*, 2023.

[3] He-Liang Huang, Dachao Wu, Daojin Fan, and Xiaobo Zhu. Superconducting quantum computing: a review. *Science China Information Sciences*, 63:1–32, 2020.

[4] Long B Nguyen, Yen-Hsiang Lin, Aaron Somoroff, Raymond Mencia, Nicholas Grabon, and Vladimir E Manucharyan. High-coherence fluxonium qubit. *Physical Review X*, 9(4):041041, 2019.

[5] Quentin Ficheux, Long B Nguyen, Aaron Somoroff, Haonan Xiong, Konstantin N Nesterov, Maxim G Vavilov, and Vladimir E Manucharyan. Fast logic with slow qubits: microwave-activated controlled-z gate on low-frequency fluxoniums. *Physical Review X*, 11(2):021026, 2021.

[6] SE Rasmussen, KS Christensen, SP Pedersen, LB Kristensen, T Bækkegaard, NJS Loft, and NT Zinner. Superconducting circuit companion—an introduction with worked examples. *PRX Quantum*, 2(4):040204, 2021.

[7] Guanyu Zhu, David G Ferguson, Vladimir E Manucharyan, and Jens Koch. Circuit qed with fluxonium qubits: Theory of the dispersive regime. *Physical Review B*, 87(2):024510, 2013.

[8] Jedediah Edward Jensen Johnson. *Optimization of superconducting flux qubit readout using near-quantum-limited amplifiers*. University of California, Berkeley, 2012.

[9] Michelle Moreno. Kerr effect. *São Carlos, Brazil: Instituto de Física de São Carlos-Universidade de São Paulo*, 4, 2018.

[10] FJ Hyde. Varactor-diode parametric amplifiers. *Electronics and Power*, 10(6):197–198, 1964.

[11] Jose Aumentado. Superconducting parametric amplifiers: The state of the art in josephson parametric amplifiers. *IEEE Microwave magazine*, 21(8):45–59, 2020.

[12] Chris Macklin, K O'brien, D Hover, ME Schwartz, V Bolkhovsky, X Zhang, WD Oliver, and I Siddiqi. A near–quantum-limited josephson traveling-wave parametric amplifier. *Science*, 350(6258):307–310, 2015.

[13] Luca Fasolo, Angelo Greco, Emanuele Enrico, Fabrizio Illuminati, Rosario Lo Franco, David Vitali, and Patrizia Livreri. Josephson traveling wave parametric amplifiers as non-classical light source for microwave quantum illumination. *Measurement: Sensors*, 18:100349, 2021.

[14] Philipp Krüger and Kirill G Fedorov. Fortgeschrittenenpraktikum: The josephson parametric amplifier, 2021.

[15] Christopher Eichler and Andreas Wallraff. Controlling the dynamic range of a josephson parametric amplifier. *EPJ Quantum Technology*, 1:1–19, 2014.

[16] Lukas Johannes Splitthoff and Christian Kraglund Andersen. Building and characterizing a parametric amplifier. 2023.

[17] Daniel Manzano. A short introduction to the lindblad master equation. *Aip Advances*, 10(2), 2020.

[18] Aashish A Clerk, Michel H Devoret, Steven M Girvin, Florian Marquardt, and Robert J Schoelkopf. Introduction to quantum noise, measurement, and amplification. *Reviews of Modern Physics*, 82(2):1155, 2010.

[19] Chenxu Liu, Tzu-Chiao Chien, Michael Hatridge, and David Pekker. Optimizing josephson-ring-modulator-based josephson parametric amplifiers via full hamiltonian control. *Physical Review A*, 101(4):042323, 2020.

[20] Ananda Roy and Michel Devoret. Quantum-limited parametric amplification with josephson circuits in the regime of pump depletion. *Physical Review B*, 98(4):045405, 2018.

[21] Mohammad Khalifa and Joseph Salfi. Nonlinearity and parametric amplification of superconducting nanowire resonators in magnetic field. *Physical Review Applied*, 19(3):034024, 2023.

[22] Tsuyoshi Yamamoto, K Inomata, M Watanabe, K Matsuba, T Miyazaki, William D Oliver, Yasunobu Nakamura, and JS Tsai. Flux-driven josephson parametric amplifier. *Applied Physics Letters*, 93(4), 2008.

[23] Nihad Ibrahim Dib. *Theoretical characterization of coplanar waveguide transmission lines and discontinuities*. University of Michigan, 1992.

[24] A Yu Levochkina, HG Ahmad, P Mastrovito, I Chatterjee, D Massarotti, D Montemurro, F Tafuri, GP Pepe, and M Esposito. Numerical simulations of josephson traveling wave parametric amplifiers (jtwpas): comparative study of open-source tools. *IEEE Transactions on Applied Superconductivity*, 2024.

[25] B Nataraj and KR Prabha. Analysis and modeling of various tapered coplanar waveguide. In *IOP Conference Series: Materials Science and Engineering*, volume 1084, page 012044. IOP Publishing, 2021.

[26] Matthew A Franzi, Sami Tantawi, Valery Dolgashev, Erik Jongewaard, and John Eichner. Novel high-power microwave circulator employing circularly polarized waves. *IEEE Transactions on Plasma Science*, 48(6):1984–1992, 2020.

[27] Hossein Mehrpour Bernety, Luc S Houriez, Jesse A Rodríguez, Benjamin Wang, and Mark A Cappelli. A tunable microwave circulator based on a magnetized plasma as an active gyrotropic element. *Physics of Plasmas*, 29(11), 2022.

[28] Firouzeh Ebadi, Nima Taghavinia, Raheleh Mohammadpour, Anders Hagfeldt, and Wolfgang Tress. Origin of apparent light-enhanced and negative capacitance in perovskite solar cells. *Nature communications*, 10(1):1574, 2019.

[29] Benjamin Lienhard, Jochen Braumüller, Wayne Woods, Danna Rosenberg, Greg Calusine, Steven Weber, Antti Vepsäläinen, Kevin O'Brien, Terry P Orlando, Simon Gustavsson, et al. Microwave packaging for superconducting qubits. In *2019 IEEE MTT-S International Microwave Symposium (IMS)*, pages 275–278. IEEE, 2019.

[30] Sihao Huang, Benjamin Lienhard, Greg Calusine, Antti Vepsäläinen, Jochen Braumüller, David K Kim, Alexander J Melville, Bethany M Niedzielski, Jonilyn L Yoder, Bharath Kannan, et al. Microwave package design for superconducting quantum processors. *PRX Quantum*, 2(2):020306, 2021.

[31] Time-Harmonic Electromagnetic Fields. *Time harmonic electromagnetic fields*. McGraw-Hill, 1961.

[32] Ravikumar Sanapala. *Characterization of FR-4 printed circuit board laminates before and after exposure to lead-free soldering conditions*. University of Maryland, College Park, 2008.

[33] Elaine Liew, Mitsui Copper Foil Malaysia, Shah Alam Malaysia, Taka Aki Okubo, Toshio Sudo, Toshihiro Hosoi, Hiroaki Tsuyoshi, and Fujio Kuwako. Signal transmission loss due to copper surface roughness in high-frequency region. In *Proc. IPC APEX EXPO*, 2014.

[34] Leonardo Ranzani, Guilhem Ribeill, Brian Hassick, and Kin Chung Fong. Wideband josephson parametric amplifier with integrated transmission line transformer. In *2022 IEEE International Conference on Quantum Computing and Engineering (QCE)*, pages 314–319. IEEE, 2022.

[35] Christopher Eichler, Y Salathe, J Mlynek, S Schmidt, and A Wallraff. Quantum-limited amplification and entanglement in coupled nonlinear resonators. *Physical review letters*, 113(11):110502, 2014.

[36] S. Gallagher and W.J. Gallagher. The spherical resonator. *IEEE Transactions on Nuclear Science*, 32(5), 1985.

[37] RA Yadav and ID Singh. Normal modes and quality factors of spherical dielectric resonators: I—shielded dielectric sphere. *Pramana*, 62:1255–1271, 2004.